Controlling Atom-Photon Bound States in an Array of Josephson-Junction Resonators

Marco Scigliuzzo[,1,*] Giuseppe Calajò[,2] Francesco Ciccarello[,3,4] Daniel Perez Lozano[,1] Andreas Bengtsson[,1] Pasquale Scarlino[,5,6] Andreas Wallraff[,7,8] Darrick Chang[,2,9] Per Delsing[,1] and Simone Gasparinetti[1,7,†]

[1]*Department of Microtechnology and Nanoscience, Chalmers University of Technology, 412 96 Gothenburg, Sweden*
[2]*ICFO-Institut de Ciencies Fotoniques, The Barcelona Institute of Science and Technology, 08860 Castelldefels (Barcelona), Spain*
[3]*Universitá degli Studi di Palermo, Dipartimento di Fisica e Chimica, I-90123 Palermo, Italy*
[4]*NEST, Istituto Nanoscienze-CNR, Piazza S. Silvestro 12, 56127 Pisa, Italy*
[5]*Institute of Physics, Ecole Polytechnique Federale de Lausanne, 1015 Lausanne, Switzerland*
[6]*Center for Quantum Science and Engineering, Ecole Polytechnique Fédérale de Lausanne (EPFL), CH-1015 Lausanne, Switzerland*
[7]*Department of Physics, ETH Zürich, CH-8093 Zürich, Switzerland*
[8]*Quantum Center, ETH Zürich, 8093 Zürich, Switzerland*
[9]*ICREA-Institució Catalana de Recerca i Estudis Avançats, 08010 Barcelona, Spain*

Engineering the electromagnetic environment of a quantum emitter gives rise to a plethora of exotic light-matter interactions. In particular, photonic lattices can seed long-lived atom-photon bound states inside photonic band gaps. Here, we report on the concept and implementation of a novel microwave architecture consisting of an array of compact superconducting resonators in which we have embedded two frequency-tunable artificial atoms. We study the atom-field interaction and access previously unexplored coupling regimes, in both the single- and double-excitation subspace. In addition, we demonstrate coherent interactions between two atom-photon bound states, in both resonant and dispersive regimes, that are suitable for the implementation of SWAP and CZ two-qubit gates. The presented architecture holds promise for quantum simulation with tunable-range interactions and photon transport experiments in the nonlinear regime.

Subject Areas: Atomic and Molecular Physics
Condensed Matter Physics
Quantum Information

I. INTRODUCTION

Quantum emitters coupled to structured photonic environments constitute both an emerging paradigm of quantum optics [1,2] and a promising platform for quantum information processing [3–6] and quantum simulation of many-body physics [7–10]. One-dimensional photonic lattices modify the electromagnetic environment, leading to the appearance of finite bands and band gaps in the energy spectrum. A major phenomenon in these systems is the formation of atom-photon bound states in the photonic band gaps [11–21]. These states originate from the dressing of the atom with a photonic cloud that remains exponentially localized in its

vicinity, thus inhibiting a full atomic decay. In addition, when multiple atoms are coupled to the same photonic lattice to form atom-photon bound states, their interaction is mediated by the overlap of their photonic wave functions. Since the photonic localization length can be controlled by varying either the frequency of the atom or the strength of its coupling to the lattice, this architecture supports tunable-range interactions, opening opportunities for quantum simulation of exotic spin models [22–25] and quantum computing architectures with connectivity beyond the nearest neighbor [26].

Atom-photon bound states have been observed in different systems, ranging from cold atoms coupled to photonic crystal waveguides [27], to optical lattices [28,29], to superconducting circuits [30,31]. A seminal experiment in superconducting circuits [30] relied on a microwave photonic crystal consisting of a coplanar waveguide with periodically modulated impedance. In a photonic crystal, the lattice periodicity must be of the same order as the wavelength of the radiation in the band gap. At microwave frequencies, this constraint results in a large footprint, which limits the number of unit cells that can be accommodated on a chip to a dozen and hinders the integration of

[*]marco.scigliuzzo.physics@gmail.com
[†]simoneg@chalmers.se

additional measurement and control circuitry. A new avenue was opened by the introduction of superconducting metamaterials with a deep subwavelength lattice constant, consisting of a set of lumped-element resonators periodically loading a transmission line, or arranged in a linear chain to form a coupled-cavity array [32–34]. In these embodiments, the lattice footprint is drastically reduced (nearly 2 orders of magnitude), and the photonic cloud is more strongly confined. In addition, by staggering the hopping amplitudes between neighboring resonators, lattices with nontrivial topology have been realized, which host topologically protected bound states [34].

Here, we introduce a novel circuit quantum electrodynamics (QED) implementation of photonic lattices coupled to quantum emitters, which employs arrays of Josephson-junction resonators and transmon qubits. Compared to previous work, our implementation features a reduced footprint, an enhanced interaction strength, and a higher extensibility. These benefits are obtained by increasing the impedance of the resonators compared with previous realizations, utilizing arrays of Josephson junctions as compact inductors in the resonator array [35–37].

The geometry of our resonator array facilitates the arrangement of time-domain and frequency control circuitry for the qubits. This capability enables the exploration of individual atom-photon bound-state properties. We present spectroscopy and time-domain measurements of a proof-of-principle device comprising an array of 21 high impedance resonators and two transmon qubits with dedicated measurement and control circuitry. We characterize the mode structure of the array and the emergence of atom-photon bound states. Using time-domain measurements, we gain unique insight regarding the structure of the atom-photon bound state by extracting the mixing angle between atomic and photonic components and by measuring the anharmonicity renormalization. We also present original numerical results that highlight the interplay between double-atomic and double-photonic excitations in the double-excitation manifold. Finally, we observe fast, coherent population exchange between two atom-photon bound states, and we report the cross-Kerr (ZZ) interaction between two atom-photon bound states, which is inaccessible with coherent driving spectroscopy.

Our results demonstrate that the presented architecture is endowed with all essential building blocks to carry out quantum simulation and quantum information processing tasks, and to access nonlinear regimes of quantum optics. The foreseen possibility to accommodate multiple emitters with a limited increase in physical footprint looks particularly promising for carrying out quantum simulations of large many-body spin Hamiltonians [22].

II. RESULTS

A. Sample and experimental setup

We implement the structured photonic environment as a transmission line made out of 21 high-impedance

microwave resonators forming a coupled-cavity array (Fig. 1). Each resonator consists of an array of ten Josephson junctions of total inductance $L_r = 8.87$ nH shunted by a capacitor $C_r = 91.3$ fF, resulting in a bare resonant frequency $\omega_r = 5.593$ GHz and a characteristic impedance $Z_r = 312 \, \Omega$. Nearest-neighbor resonators are capacitively coupled to form a linear chain, and each edge resonator is coupled to a 50-Ω coplanar waveguide. The artificial atoms (Q_1 and Q_2) are implemented as superconducting flux tunable transmons [38] capacitively coupled to sites 10 and 12 of the array. Each transmon is additionally coupled to a charge line (XY control), a flux line (Z control), and a readout resonator. The device is realized in aluminum on a silicon substrate with a standard lithographic process [39]. The sample is wire bonded to a copper sample holder thermally anchored to the mixing chamber stage of a dilution refrigerator at 10 mK. A summary of the relevant sample parameters and further experimental details are presented in Appendix A.

B. Transmission spectroscopy of the array

1. Bare coupled cavity array

To characterize the bare coupled cavity array, we tune the resonant frequencies of Q_1 and Q_2 far away from the transmission band and measure the transmission coefficient through the array (Fig. 2). At low driving powers (average photon number in the array mode $n \approx 1$), a structure of $N = 21$ modes forming a passband emerges in the transmission spectrum, from the first mode at $\omega_1/2\pi = 5.219$ GHz to the last one at $\omega_{21}/2\pi = 6.215$ GHz. These modes present rather uniform spacing and linewidths in the center of the band, while they concentrate and become narrower in the linewidth at the band edges. These features are captured by a tight-binding model for the array with only three parameters: the single-cavity bare resonance frequency ω_r, the cavity-cavity nearest-neighbor coupling J, and the coupling of the edge cavities to the input and output transmission lines, κ (see Appendix B). In the limit $\kappa \ll J$, which applies here, the resonance frequencies of the modes are given by

$$\omega_k = \omega_r + 2J \cos\left(\frac{\pi k}{N+1}\right) \quad k = 1, \ldots, N, \quad (1)$$

the linewidth of each being

$$\kappa_k = \frac{2\kappa}{N+1} \sin^2\left(\frac{k}{2}\right). \quad (2)$$

Equation (1) predicts a passband of width $4J$ centered around the bare cavity frequency ω_r. From Eq. (1), $4J \approx \omega_{21} - \omega_1$, and we extract $J/2\pi = 249$ MHz. Comparing it to previous realizations of microwave coupled cavity arrays [33,34], we achieve a larger value for J with a smaller coupling capacitance, thanks to the higher impedance of the resonator
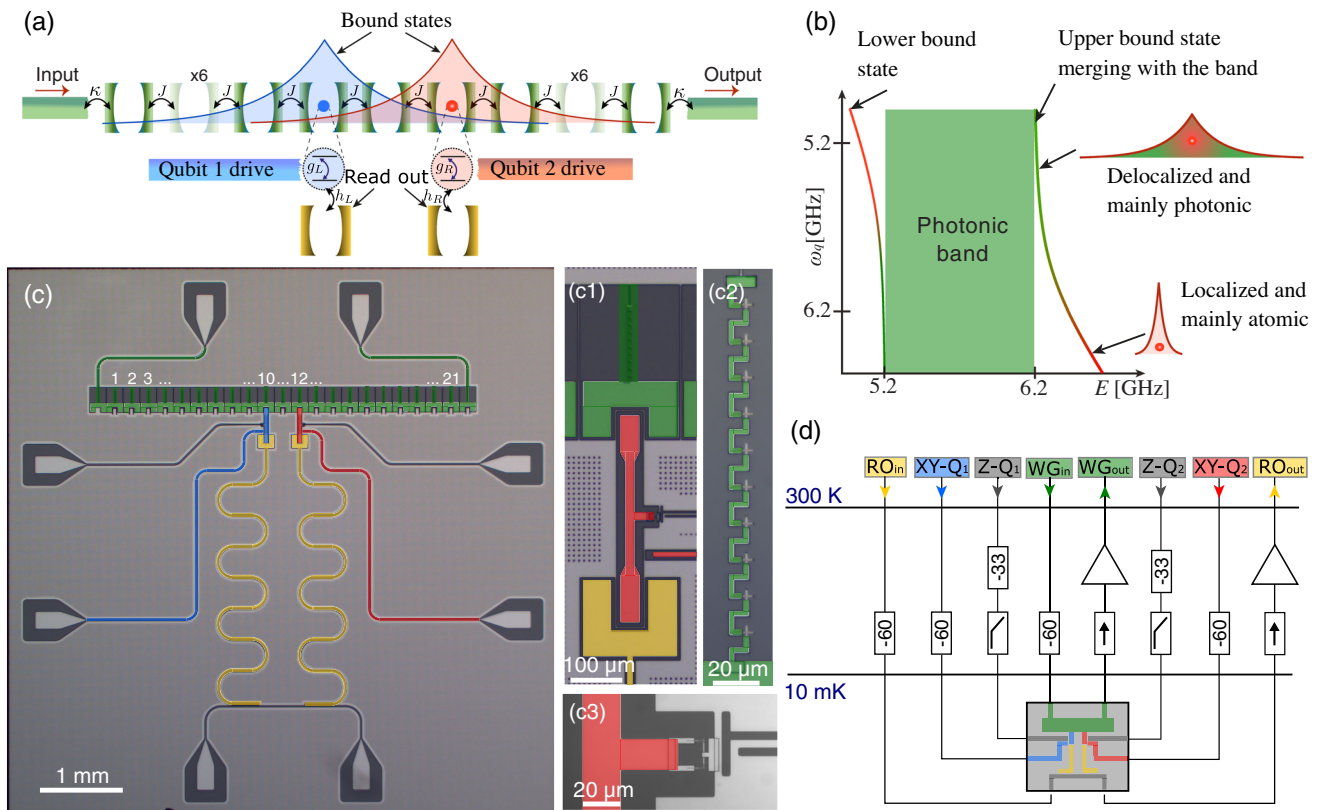
FIG. 1. Two artificial atoms interacting with a coupled-cavity array. (a) Concept: qubit 1, Q_1 (blue), and qubit 2, Q_2 (red), are locally coupled to an array of 21 cavities (green). Each atom can be independently controlled through an individual driving line (same color as the atom) and its state measured via a dedicated readout resonator (yellow). Each qubit is dressed by a photon, giving rise to a corresponding atom-photon bound state (see shaded cloud localized around each atom). (b) Energy diagram of dressed states as a function of the bare qubit frequency ω_q. For a fixed ω_q, the bound state emerges as a discrete energy E separated from the photonic band (green shaded region). The color scale of the bound state (from green to red) indicates whether the excitation is mostly photonic or atomic in nature. (c) Micrograph of the sample and (d) simplified experimental setup: An array of 21 Josephson-junction (JJ) resonators (green) is capacitively coupled at its edges to coplanar waveguides directly connected to the input (WG$_{in}$) and output (WG$_{out}$) of two cryostat lines. The transmon qubits Q1 and Q2 are coupled to resonator (cavity) 10 and 12, respectively, and driven through dedicated charge lines XY-Q$_1$ and XY-Q$_2$, respectively. Each qubit state is detected through 2 quarter-wavelength coplanar resonators (yellow) inductively multiplexed on a transmission line measured through RO$_{in}$ and RO$_{out}$. The qubit frequencies are tuned by injecting a magnetic flux in the transmon SQUID loop with individual flux lines (Z-Q$_1$ and Z-Q$_2$). Details of the JJ resonator and Q_2, the JJ array, and the Q$_2$ SQUID and flux line are shown in panels (c1)–(c3), respectively.

$(J = \frac{1}{2} C_J \omega_r^2 Z_r)$. From electrostatic simulations, we estimate the resonator impedance to be $Z_r = 1/\omega_r C_r \approx 312$ Ω. This implies a sixfold gain on the capacitive coupling strength compared with 50-Ω resonators.

Compared to the predictions of this simple model, the measured traces present deviations in the frequency distribution of the modes, which we attribute to a 3% scatter in the resistance of the fabricated Josephson junctions [40], resulting in an estimated standard deviation of $\delta\omega_r/2\pi = 25$ MHz in the frequencies of the bare (uncoupled) resonators in the array. Importantly, thanks to the small ratio $\delta\omega_r/J = 1/10$, this frequency disorder does not significantly affect the properties of the atom-photon bound states, as calculated by numerical diagonalization of the system Hamiltonian for various realizations of the disorder

and directly verified in our experiments below. In addition, we measure a nonzero transmission outside the photonic passband and an alternating transmission background in between resonant modes, which we ascribe to direct crosstalk between the input and output ports of our sample box. For a detailed treatment of these experimental imperfections, see Appendix C.

At higher powers, corresponding to $n \sim 10^2$, each individual mode exhibits the typical phenomenology of a Kerr resonator, due to the nonlinearity inherited by the arrays of Josephson junctions [41]. In our design, we estimate the Kerr coefficient for a single mode to be $K/2\pi = 100$ kHz, much smaller than the mode linewidth. In fact, the frequency shift produced by more than 100 photons is still smaller than a linewidth, as visible in
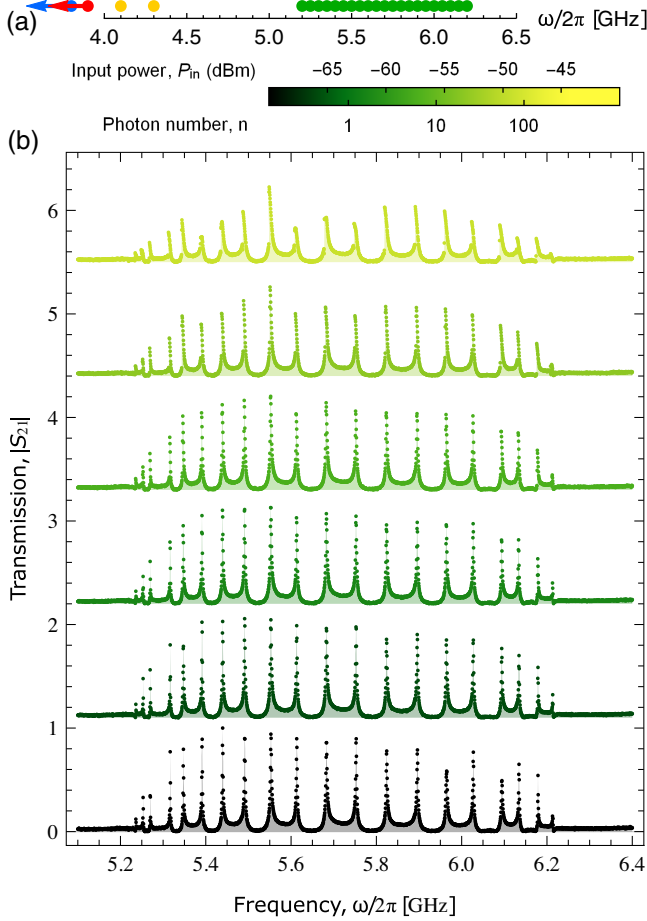
FIG. 2.　Single coherent tone spectroscopy of the coupled cavity array. (a) Frequency landscape of the resonant modes of the systems: Q_1 (blue), Q_2 (red) (tuned away from the band in this measurement), readout resonators (yellow), and array modes (green). (b) Transmitted amplitude, $|S_{21}|$ vs frequency, ω, for different input powers, and P_{in} at room temperature. The traces are vertically offset in steps of 1.1 and filled to their own baseline for clarity.

Fig. 2(b). Importantly, this value can be determined by design, by choosing the number of junctions in a single resonator or the number of unit cells in the resonator array. The extraction of this parameter and the relation between the Kerr coefficient of individual resonators and that of the array modes are discussed in Appendix A 3. In the remainder of this work, we only consider the linear regime of the coupled cavity array.

2. Dressed coupled cavity array and atom-photon bound states

We characterize the interaction of each qubit with the coupled cavity array by tuning its frequency across the passband while keeping the other qubit detuned [Fig. 3(a)]. Here, we discuss the results for Q_2; the results for Q_1 are comparable (see Appendix A 2).

The low-power transmission coefficient of the array is affected by the presence of the qubit [Fig. 3(b)]. We observe a minimum in transmission within the band in correspondence with the bare qubit frequency [red dashed line in Fig. 3(b)]. In fact, in the low excitation regime, the incoming field is coherently scattered back [42]. This effect is particularly visible when the bare qubit frequency is resonant with one of the coupled-cavity array modes. In Sec. II C, we show that an atom-cavity interaction strength is approximately $g_i/2\pi \sim 300$ MHz, 5 times larger than the frequency spacing of the modes, implying a multimode interaction [43]. In particular, the absence of an avoided crossing between a single mode and the artificial atom, and the monotonic dispersive shift of a mode, indicate the interaction of the artificial atom with multiple modes. Moreover, each mode presents a definite standing-wave spatial profile, which sets its effective interaction strength with the artificial atom. For example, mode $m = 10$, indicated by the white arrow in Figs. 3(b) and 3(c), is completely decoupled from the qubit due to a corresponding node on the site of the artificial atom.

Comparing our system with a previous realization of multimode strong coupling [44], the vanishing group velocity v_g at the band edges produces a nontrivial density of photonic states, proportional to $1/v_g$ [45]. As the atom frequency approaches the band, it hybridizes with band-edge photons having zero velocity [17,30]. This seeds an evanescent field, exponentially localized around the atom [shaded area around the atoms in Fig. 1(a)]. In Fig. 3(d), we observe this additional photonlike mode outside the passband, which asymptotically approaches the band edge when the bare qubit frequency is moved towards the center of the band.

To model the transmission spectra, we introduce the Hamiltonian

$$H/\hbar = \sum_{x=1}^{N} \omega_r a_x^\dagger a_x + \sum_{x=1}^{N-1} J(a_x^\dagger a_{x+1} + a_{x+1}^\dagger a_x)$$
$$+ \sum_{i=1}^{2} \omega_{qi} b_i^\dagger b_i + \frac{1}{2}\beta_i b_i^\dagger b_i^\dagger b_i b_i + g_i(a_{x_i}^\dagger b_i + b_i^\dagger a_{x_i}),$$

$$(3)$$

where we introduce the photon annihilation operator a_x for the xth cavity, the transition frequencies ω_{qi} of qubits Q_i, their anharmonicities β_i, and finally their couplings with the x_ith cavity, g_i. We calculate the transmission coefficient in the limit of linear response from input-output theory and find a qualitative agreement with our measurements [Fig. 3(c); see Appendix B 6 for details].

When the frequency of the qubit is tuned towards the low-frequency edge of the band, the bound state at higher frequency (upper bound state) completely loses its atomic nature, becoming the mode at the high-frequency edge of
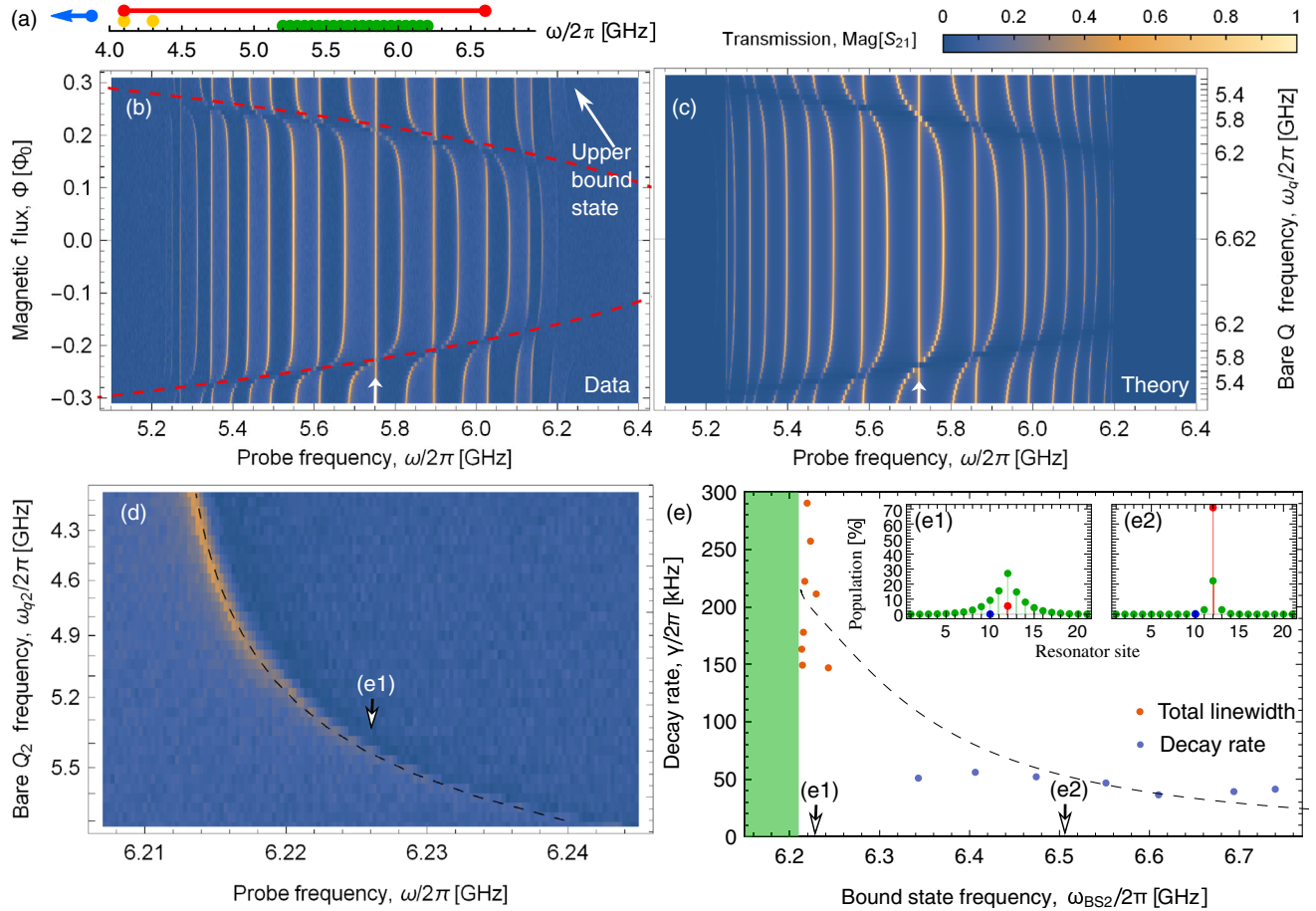
FIG. 3. Single coherent tone spectroscopy as a function of Q_2 frequency. (a) Frequency landscape: Q_1 is tuned to its lowest frequency. The Q_2 frequency is tuned from its largest frequency at 6.6 GHz to 4.1 GHz. (b) Low-power coherent tone spectroscopy through the resonator array as a function of the Q_2 frequency (dashed red line). (c) Calculated transmission spectrum via input-output theory using the single-excitation Hamiltonian Eq. (3). (d) Detail of the measurement in panel (a) showing how the atom-photon bound state approaches the band and eventually becoming the last array modes. The dashed black line shows data fit via Eq. (4). (e) Total decay rate of the bound state as a function of its frequency. The red data are obtained from the transmission spectroscopy, while the blue are from the atom spectroscopy (see Sec. II C). The dashed black line represents the theoretically expected decay rate. Insets: calculated distribution of the excitation over the array (green dots) and between the two qubits (blue and red, respectively) for two distinct bound-state frequencies: $\omega_{BS2} = 6.226$ GHz (e1) and $\omega_{BS2} = 6.510$ GHz (e2).

the band. Conversely, the mode at the low-frequency edge starts to get dressed with an atomic component [lower bound state, barely visible in Fig. 3(b)], as predicted by the Hamiltonian (3) for a single qubit.

Their frequencies ω_{BSi} ($i = 1, 2$ for Q_1 and Q_2, respectively) are given by the solutions of the equation

$$\omega_{BSi} - \omega_{qi} = \frac{g^2}{(\omega_{BSi} - \omega_r)\sqrt{1 - \frac{4J^2}{(\omega_{BSi} - \omega_r)^2}}}, \qquad (4)$$

with $\omega_{BSi} - \omega_r > 2J$ (see Appendix B 3 for more details). The upper bound state will be our main focus for the rest of the paper, and we use its frequency as the independent variable to describe our measurements. As pictorially shown in Fig. 1(b), this state is highly localized and

atomlike in nature for atomic bare frequency deep in the gap, while it is more photonlike and delocalized for atomic frequency close to the passband. These features are directly exploited for exciting the bound state: The finite overlap of the photonic cloud with the resonators at the edges of the array allows for the detection of this state in transmission [see Figs. 3(b)–3(d)].

The decay rate of the bound state, extracted from the linewidth of the transmission spectroscopy as a function of the bound-state frequency, is of the order of $\gamma/2\pi \approx 300$ kHz, close to the decay rate of the array modes [Fig. 3(e), orange dots], due to the large and delocalized photonic component of the bound state [Fig. 3(e1)]. When the bound state is far from the band, we extract its decay rate from a measurement of its atomic component via the readout resonators. In this case, the losses are much smaller

[Fig. 3(e)] due to the mainly atomic component [Fig. 3(e2)], and we measure a decay rate $\gamma/2\pi \approx 50$ kHz.

C. State preparation of a single atom-photon bound state

1. Single-excitation subspace

In the limit in which the atom-photon bound state is localized, and thereby not accessible by transmission spectroscopy of the array, we excite it by sending microwave pulses to the qubit via its charge line and detect it by performing dispersive qubit readout using the readout resonators [see Fig. 1(c1) and pulse scheme in Fig. 4(a)]. A 90-ns Gaussian pulse with frequency ω_p and an amplitude calibrated to be π pulse when Q_2 is at its maximum frequency, $\omega_{q2,m}$, is sent to the XY-Q_2 control line (red). At the same time, the frequency of Q_2, ω_{q2}, is set with a 140-ns square pulse (with a 2-ns rise and 2-ns fall time) on the magnetic flux control, $Z - Q_2$ with varying amplitude Φ_{q2} (gray line and red shaded area). The frequency of Q_1 is dynamically tuned to its lowest value with a flux pulse of half-flux quantum $\Phi_0/2$. After 50 ns, a $2 - \mu$s square readout pulse sent to the multiplexed resonators is used to read out the average qubit population P_2. The excitation spectrum of the bound state is obtained by measuring P_2 as a function of pulse frequency and magnetic flux applied to Q_2 [Fig. 4(b)]. When the pulse on XY-Q_2 is resonant with the bound-state transition frequency, the qubit is efficiently excited. The bound-state frequency strongly differs from the bare qubit frequency [red dashed line in Fig. 4(b)] and asymptotically approaches the band edge for qubit frequencies in the band [Fig. 4(c)]. In this case, the bound-state frequency is also well described by the continuum theory, as shown by the solid black line in Fig. 4(b), representing the best fit of Eq. (4) to the data. We notice that, keeping the pulse amplitude constant, the bound-state population decreases as its frequency approaches the band edge. Compared to the drive rate $\Omega_{R,0}$ for an isolated qubit excited via its charge line by a pulse of given amplitude, the bound state is subject to a reduced drive rate $\Omega_R = \Omega_{R,0} \cos(\theta)$, where θ is the mixing angle between the atomic and photonic components. This relation allows us to extract the mixing angle from the measurements in Fig. 4(b), which we find to be in good agreement with our theoretical prediction [Fig. 4(d)].

2. Double-excitation subspace

The physics of the bound states explored so far was restricted to a single excitation. When higher-excitation subspaces are considered, the nonlinear nature of the transmon starts to play a role and leads to deviations from the linear regime. To explore these nonlinear features, we "climb up" to the two-excitation subspace using a sequence of two pulses [Fig. 5(a)]. We first send a resonant π pulse to excite the long-lived, single-excitation bound state. We subsequently send another pulse of fixed amplitude and
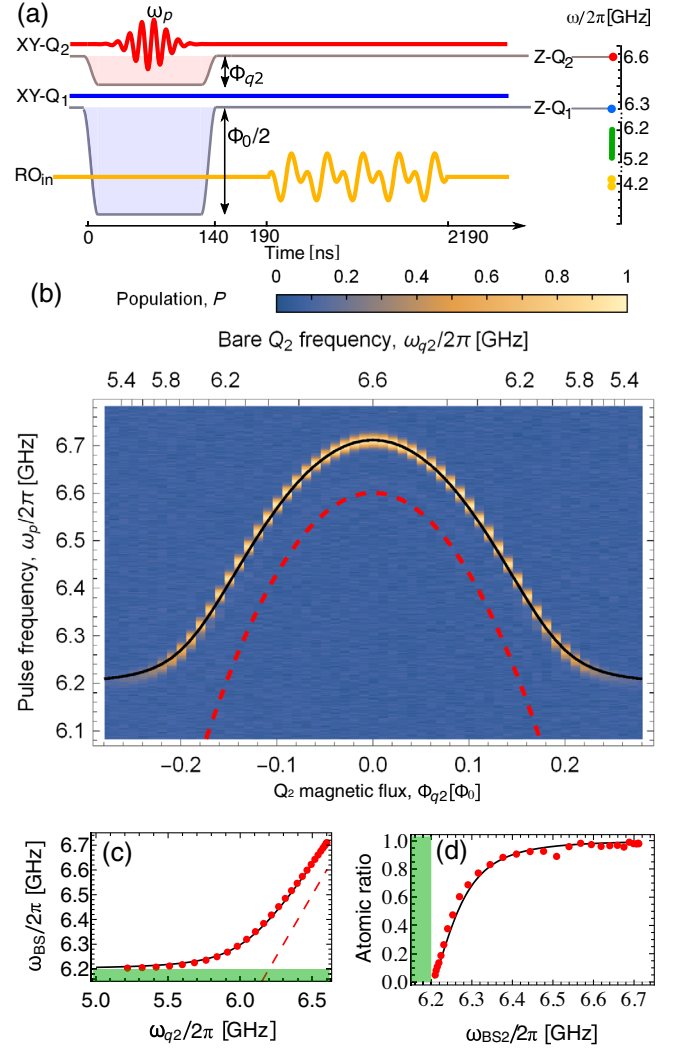

FIG. 4. Isolated bound state in single excitation subspace. (a) Pulse scheme. A Gaussian pulse (red line) with frequency ω_p drives Q_2, while Q_1 is far detuned by the flux pulse (blue shaded area). The readout pulse (in yellow) reads the population in both qubits. On the side, Q_1 and Q_2 (blue and red dots, respectively), the photonic band (green dots), and the readout resonator (yellow dots) frequencies are depicted in relation to the flux pulses. (b) Population of Q_2 as a function of flux pulse amplitude Φ_{q2} and driving pulse frequency ω_p. The black line shows the fit of the bound-state frequency given in Eq. (4) as a function of the expected bare Q_2 frequency (red dashed line). (c) Bound-state frequency extracted from panel (b). (d) Atomic fraction of the excitation. The black line shows the expected value [Eq. (B24)] using the parameters extracted from the fit in panels (b) and (c).

varying frequency ω_{p2} to search for the first-to-second-excited-state transition of the bound state. Finally, because our readout pulses are optimized so that the ground state is the most distinguishable one, we find it convenient to add a third pulse identical to the first so that, if the second pulse does not affect the bound state, then the system is brought back to the ground state. Such a scheme allows us not only
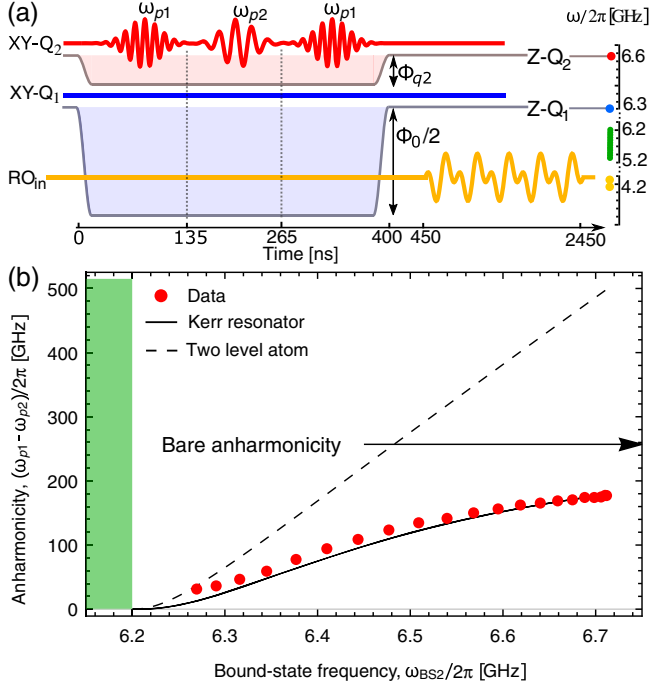
FIG. 5. Isolated bound state in the two-excitation subspace. (a) Pulse scheme. A π pulse (red line) excites Q_2, and a second Gaussian pulse brings it to the third level when ω_{p2} is resonant with the ef transition. When ω_{q2} is not resonant, a π pulse brings the qubit back to the ground state. (b) Absolute value of the dressed anharmonicity β_{dress}. The arrow indicates the value of the bare anharmonicity. The black solid line shows the calculated β_{dress}, with the parameters extracted from the fit in Fig. 4(b). Finally, the black dashed line indicates the dressed anharmonicity of an ideal two-level atom.

to perform a complete spectroscopy of the second excitation subspace but also, compared to previous approaches [31], to efficiently prepare the two excitation bound state.

In order to quantify the deviation from the linear case, we define the dressed anharmonicity parameter as $\beta_{\mathrm{dress}} = \omega_{\mathrm{BS2}}^{(2)} - 2\omega_{\mathrm{BS2}}^{(1)}$, where the superscripts (1) and (2) stand for the number of excitations. Experimentally, this quantity is determined as the difference in frequency between the second and first pulses when the second transition is resonantly excited. The measured β_{dress} is always negative; its magnitude is maximum when the bound-state frequency is the farthest from the band edge, and it monotonically decreases towards zero as the bound-state frequency approaches the band edge [Fig. 5(b), dots]. To theoretically capture the measured nonlinearity, we describe the transmon as a nonlinear resonator with bare anharmonicity $\beta/2\pi = -257$ MHz [see Eq. (3)]. This quantity is estimated by performing the same measurement as in Fig. 5(a) for $\omega_{q2}/2\pi = 3.329$ GHz, well below the band and the readout resonator frequency. We use the parameters J, ω_r, and g_1 extracted from the fit of the single excitation bound-state spectroscopy to diagonalize the Hamiltonian in the

single- and double-excitation subspace (see Appendix B 5) and to calculate the dressed anharmonicity, finding a good agreement with the measured data [Fig. 5(b), solid line].

The observed anharmonicity for the bound state is intermediate between that of a fully linear emitter, for which no anharmonicity would be observed, and that of the most nonlinear emitter, a genuine two-level atom ($\beta \to -\infty$), plotted, for comparison, as a dashed line in Fig. 5(b). A detailed numerical study, presented in Appendix B 5, indicates that double-photonic, double-atomic, and hybrid excitations are all present across the frequency range considered. In addition, we find that the localization length of the doubly excited bound state is also renormalized according to the nonlinearity of the emitter, as originally discussed in Ref. [17].

III. BOUND STATES INTERACTION

A. Two-atom bound states level splitting

To investigate the interaction between bound states, we bring their frequencies close to each other, send an excitation pulse to one of the qubits, and perform joint readout of the two qubits [Fig. 6(a)]. Sweeping the frequency of one qubit while keeping the other one fixed, we observe characteristic avoided crossings in the excitation spectrum, detected as peaks in the measured populations of both qubits as a function of the qubit and probe frequencies [Figs. 6(b)–6(g)]. Interestingly, the excitation pulse on Q_2 excites a population fraction in both bound states. In fact, when the two atom-photon bound states resonantly interact, they hybridize, forming even (+) and odd (−) states (see Appendix B 4). In Figs. 6(b)–6(g), we report the measurement results for three different frequencies of Q_1: when it is tuned well inside the band, $\omega_{q1}/2\pi \approx 5.9$ GHz [(b) and (e)]; at the band edge, $\omega_{q1}/2\pi \approx 6.2$ GHz [(c) and (f)]; and finally, at its largest bare frequency possible, $\omega_{q1}/2\pi = 6.332$ GHz [(d) and (g)].

Tuning the bound-state frequencies closer to the band edge results in a larger avoided crossing, corresponding to a larger interaction strength. It is important to notice that the two qubits do not present a direct coupling; in fact, their interaction derives from the mutual overlap of their photonic clouds, which becomes progressively more extended and populated closer to the band edge [see Figs. 3(e1) and 3(e2), where we calculated the photonic cloud distribution of the bound state depending on the distance from the band edge].

When the frequencies of the interacting bound states approach the band edge, we observe a vanishing population of the (−) bound state, when its frequency crosses the band edge [Figs. 6(b) and 6(e)]. This phenomenon, referred to as "melting" of one bound state into the modes of the band [17], only occurs in the presence of two interacting bound states, (+) and (−). The even state is characterized by a bonding behavior, and its energy is raised compared to the
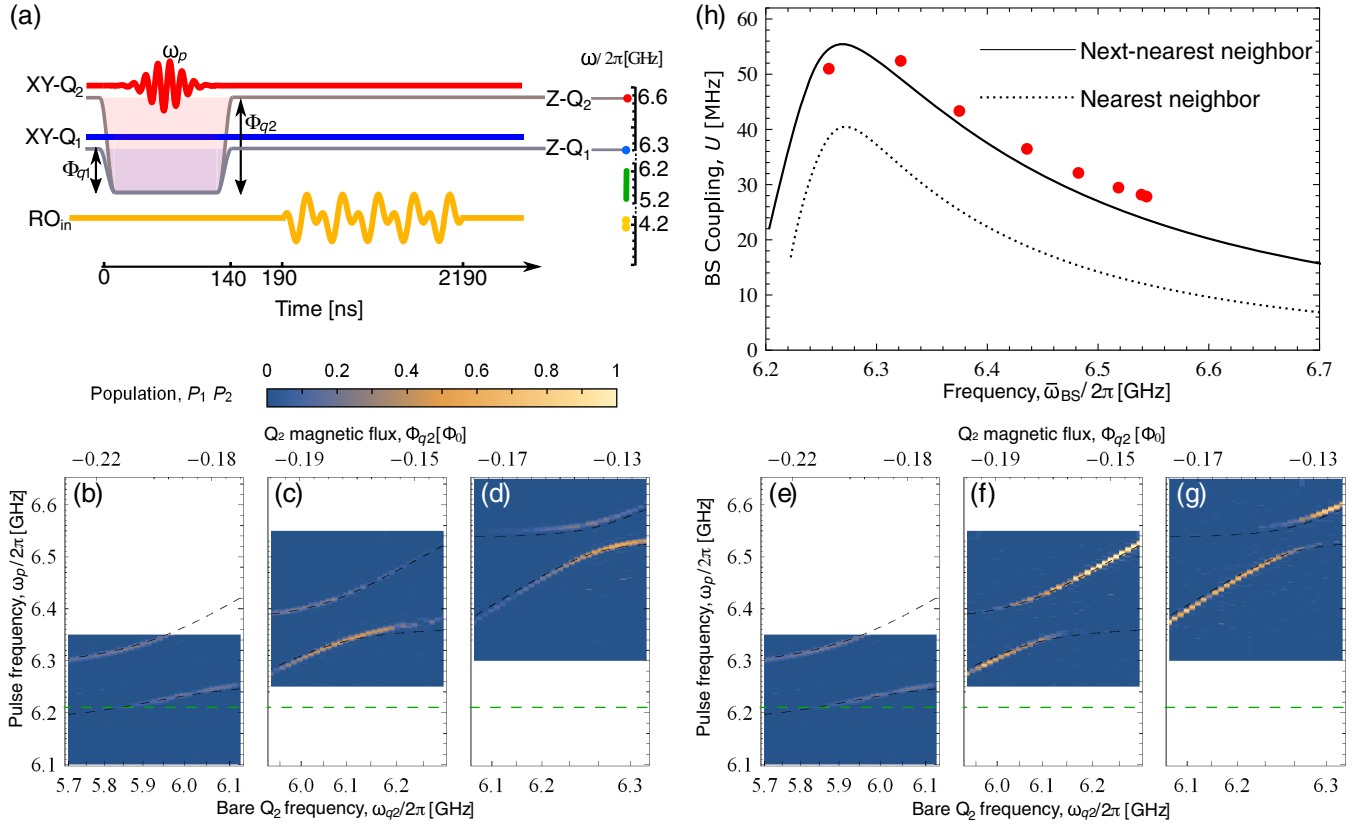
FIG. 6.   Avoided crossing and interaction strength between two bound states. (a) Pulse scheme. A Gaussian pulse (red line) with frequency ω_p drives the two bound states tuned in resonance with two flux pulses (red and blue shaded areas). The populations of the qubits are read out (yellow line) at their highest frequencies. (b)–(g) Individual bound-state population on Q_1 [P_1 (b)–(d)] and on Q_2 [P_2 (e)–(g)] as a function of the bare frequency of Q_2 for different frequencies of Q_1. The dashed black lines are the expected bound-state frequencies calculated from Hamiltonian (C1). The green dashed line indicates the photonic band edge. (h) Bound-state coupling U, as defined in the main text, extracted from the measurements reported in panels (b)–(g). The black dashed line represents the expected value calculated from the Hamiltonian Eq. (3), while the solid line is obtained by the extended model given in Eq. (C1), which takes into account the next-nearest-neighbor interaction.

one of the individual bound state, leading to an increased localization of its photonic cloud. The odd state instead presents an antibonding behavior, with its energy pushed towards the band edge, making the state more extended. This progressive delocalization leads to a disappearance of this bound-state solution.

We define the bound-state interaction strength $U = [\omega_{\mathrm{BS}+}(\omega_q) - \omega_{\mathrm{BS}-}(\omega_q)]/2$ as half of the level splitting when the bare qubit frequencies are on resonance, $\omega_q = \omega_{q1} = \omega_{q2}$, where the $\pm$ stands for even and odd dressed bound states, respectively. This quantity is displayed in Fig. 6(h) (red dots) as a function of the frequency at the midpoint of the level splitting, $\bar{\omega}_{\mathrm{BS}} = \omega_{\mathrm{BS}-} + U/2$, which gives the approximate frequency of the individual (single artificial atom) bound state. We measure the bound-state interaction strength ranging from 27 to 52 MHz in a frequency range of 250 MHz. This tunability is directly related to the variation of the overlap between the photonic clouds. Based on numerical simulation, we predict that the interaction strength could be tuned by 2 orders of

magnitude through a straightforward optimization of the device parameters (see Appendix C 2).

Figure 6(h) also shows that the coupling does not present a monotonic behavior. In fact, it increases for bound states approaching the band edge, but it exhibits a maximum close to the melting condition. This behavior relies on our definition of the BSs coupling and on the melting condition. Indeed, when the odd bound state merges with the continuum in the band, the splitting is measured between the even bound state and the band edge.

Separately, we find that the expected interaction strength calculated with the eigenvalue equation derived by the system Hamiltonian Eq. (3) (see Appendix B 4 for more details) systematically underestimates the measured coupling strength [Fig. 6(h), dotted line]. As shown in Appendix C 1, parasitic capacitances are responsible for a non-negligible coupling between each qubit and their next-nearest array sites. In particular, the bound-state interaction is affected by a direct coupling between the qubits and the cavity in between them ($x = 11$). After

including these additional couplings in the Hamiltonian, we obtain a much better agreement with the data [Fig. 6(h), solid line]. In contrast, this behavior cannot be explained by adding just a direct qubit-qubit coupling to the model.

B. Time-resolved excitation exchange

After establishing a static interaction between the bound states, we now exploit it in a dynamic setting to realize an excitation swap between two bound states [Fig. 7(a)]. When both qubits are at their largest frequencies, we excite the bound state of Q_2 with a π pulse, and we tune it in resonance with the bound state of Q_1 by applying a flux pulse on each individual flux line. After an interaction time τ, we bring the two qubits back to their initial frequencies and we read out the populations P_1 and P_2, in Q_1 and Q_2, respectively.

Figures 7(b) and 7(c) show P_1 and P_2 as a function of the bound-state interaction time τ and Q_2 frequency ω_{q2}, while the Q_1 bound-state frequency is kept at $\omega_{q1} = \omega_{q1,m}$ in panels (b) and (c), and $\omega_{q1}/2\pi = 6.15$ GHz in panels (d)–(g). These are the same parameters chosen for measuring the avoided crossing in Figs. 6(d) and 6(g). The population of the two qubits as a function of the interaction time, restricted to resonant bound states, is presented in Figs. 7(f) and 7(g). These data, corresponding to a slice of the chevron pattern [dashed blue and red lines in Figs. 7(b)–7(e)], can be fitted to a dumped sinusoidal function (solid red and blue lines), from which we extract a complete swap time of 18 ns. This value is in good agreement with the measured interaction strength.

The excitation swap between the two bound states is realized by nonadiabatically tuning the two bare bound states in resonance. The adiabatic threshold for this process is related to the interaction strength [46], with a relative time scale of about $1/U$, that corresponds to 5 ns in our implementation. The flux pulse we implement has a rise (and fall) time of $t_{\mathrm{raise}} = 1$ ns; thus, we fulfill this constraint. Nevertheless, the two bound states interact during the rise time, and we take this into account with a time shift of the measured data in Fig. 7(f).

The chevron pattern of the populations P_1 and P_2 measured for the bare frequency $\omega_{q1}/2\pi \approx 6.02$ GHz shown in Figs. 7(d) and 7(e) highlights a faster excitation swap of 13 ns, as expected from the larger interaction strength closer to the band edge. Focusing only on the resonant case [see Fig. 7(g)], we notice that after the pulse protocol, we observe a total population of only $P_1 + P_2 \sim 0.7$. The population loss originates from the weakly adiabatic regime in which we operate, i.e., $t_{\mathrm{raise}} \gtrsim 1/\Delta_{\bar{\omega}_{\mathrm{BS}}} \sim 0.5$ ns, where $\Delta_{\bar{\omega}_{\mathrm{BS}}}$ is the gap between the average individual bound-state frequency $\bar{\omega}_{\mathrm{BS}}$ and the band edge (see Sec. III A).

When the bare qubit frequency is tuned in the band faster than the latter adiabaticity threshold, the bare qubit state is not an eigenstate of the system. In this case, part of the atomic population redistributes among the resonators according to the projection of the bare qubit state on the
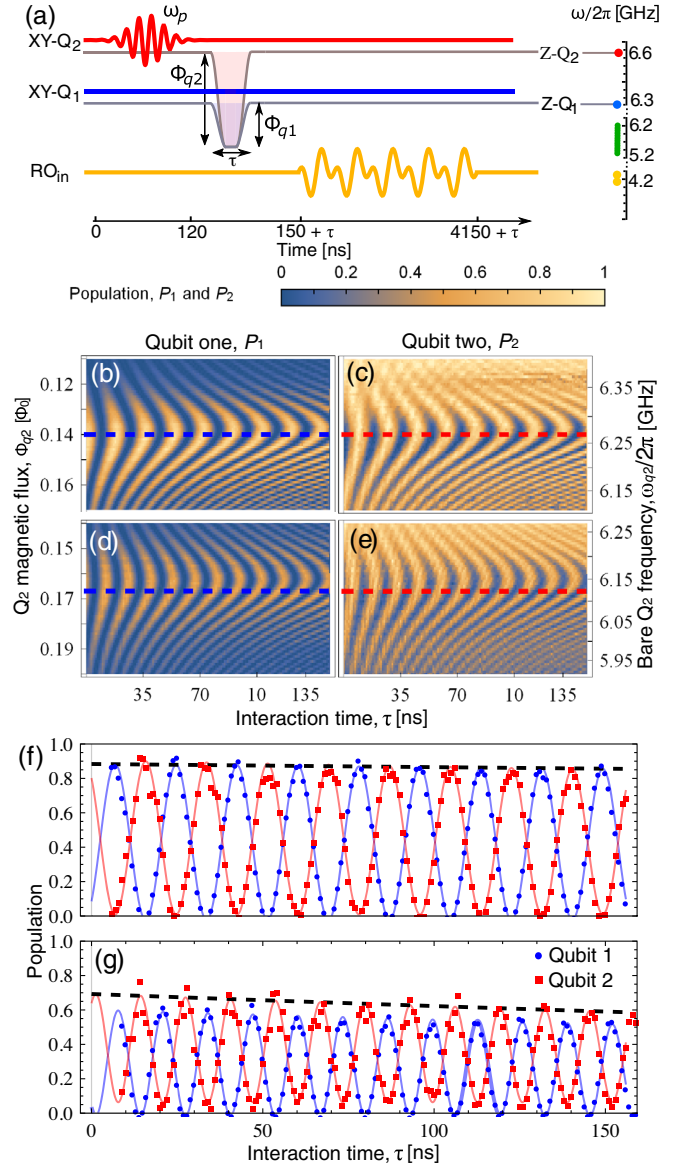

FIG. 7. Time-resolved energy swap. (a) Pulse sequence. A π pulse (red line) excites Q_2, and after 30 ns, the two bound states are tuned in resonance with two flux pulses (blue and red shaded area) for a variable duration τ. The qubits are tuned back to their unbiased frequencies, and their populations are read out (yellow line). (b)–(e) Chevron pattern. Measured bound-state population of Q_1 (left column) and Q_2 (right column) as a function of the interaction time and of the bare frequency of Q_2. The two rows correspond to two different values of ω_{q1}, at its largest frequency [(b) and (c)] and 6.02 GHz [(d) and (e)], respectively. (f,g) Horizontal line cuts in panels (b)–(e) (blue and red dashed lines) displaying the population of Q_1 (blue) and Q_2 (red) as a function of the interaction time. In both plots, the relaxation time is fitted to an exponential decay (black dashed line).

bound state. In this process, a fraction of the atomic population is converted into itinerant photons and released into the waveguide. In particular, the released population is at most $P_{\mathrm{released}} \simeq \sin^2(\theta)$, with θ being the mixing angle θ

defined in Sec. II C. In fact, where the bound states are mainly qubitlike, the total population $P_1 + P_2 \sim 0.95$ [see Fig. 7(f)], while a larger photonic dressing preserves a smaller fraction of population, $P_1 + P_2 \sim 0.7$, as shown in Fig. 7(g). This last value could be improved by slowing down the protocol but still keeping $t_{\text{raise}} \lesssim 1/U$ in order to induce the excitation swap in the first place.

The lifetime of the interaction is determined by the lifetime of the average individual bound state [dashed black lines in Fig. 7(f) and 7(g)], which we extract from the fit to be 1.2 μs and 950 ns, respectively.

C. Two-atom bound states ZZ interaction

When the two atom-photon bound states are close in frequency to the band edge, but detuned from each other, exciting one of them results in a shift in the transition frequency of the other. This ZZ (or cross-Kerr) interaction originates from dispersive and resonant interactions between energy levels in the double-excitation manifold. The interaction mechanism relies on the overlap of a photonic cloud with finite localization, as it happens in the single-excitation subspace.

We investigate the ZZ interaction with the pulse scheme displayed in Fig. 8(a). After setting the bare qubit frequencies with a flux pulse on each flux line, we excite the Q_1 bound state with a π pulse. We apply a second pulse to Q_2 with frequency ω_{p2} and finally read out the state of the qubits. When the pulse on Q_2 is such that $\omega_{p2} = \omega_{\text{BS2}}^{(2)}$, the bound state of Q_2 is excited. We repeat the same pulse sequence by tuning the bare frequency of Q_1, mapping the transition frequencies $\omega_{\text{BS2}}^{(2)}$ as a function of ω_{q1}.

Figure 8(b) shows the ZZ interaction between two excited bound states for the bound state of Q_2 tuned at the constant frequency $\omega_{\text{BS/2}}/2\pi = 6.653$ GHz, while the frequency of the Q_1 bound state is tuned from the band edge toward its largest frequency 6.55 GHz. Following the level $|\phi_{11}\rangle$ in the right panel of Fig. 8(c), we notice that this level crosses $|\phi_{02}\rangle$ relative to the two-excitation bound state of Q_2. In Fig. 8(b), at lower frequencies, we measure a residual ZZ interaction up to 49 MHz. The dashed line shows the calculated ZZ interaction numerically evaluated with the complete Hamiltonian Eq. (C1).

Note that in Ref. [31] the avoided crossing between $|\phi_{02}\rangle$ and $|\phi_{11}\rangle$ was inferred using high-power coherent spectroscopy. With this approach, second-order transitions may induce a Stark shift in the measured frequencies, while the measurement of the ZZ interaction with a pulse scheme is directly relevant for gate implementation.

Figure 8(c) shows the energy structure of bare qubits (left panel) and the same energy levels for bound states as a function of the bare frequency of Q_1. The color scale highlights the population of the two atoms going from blue for Q_1 to red for Q_2, where yellow instead stands for excitation equally distributed on the two. Figure 8(c) is a
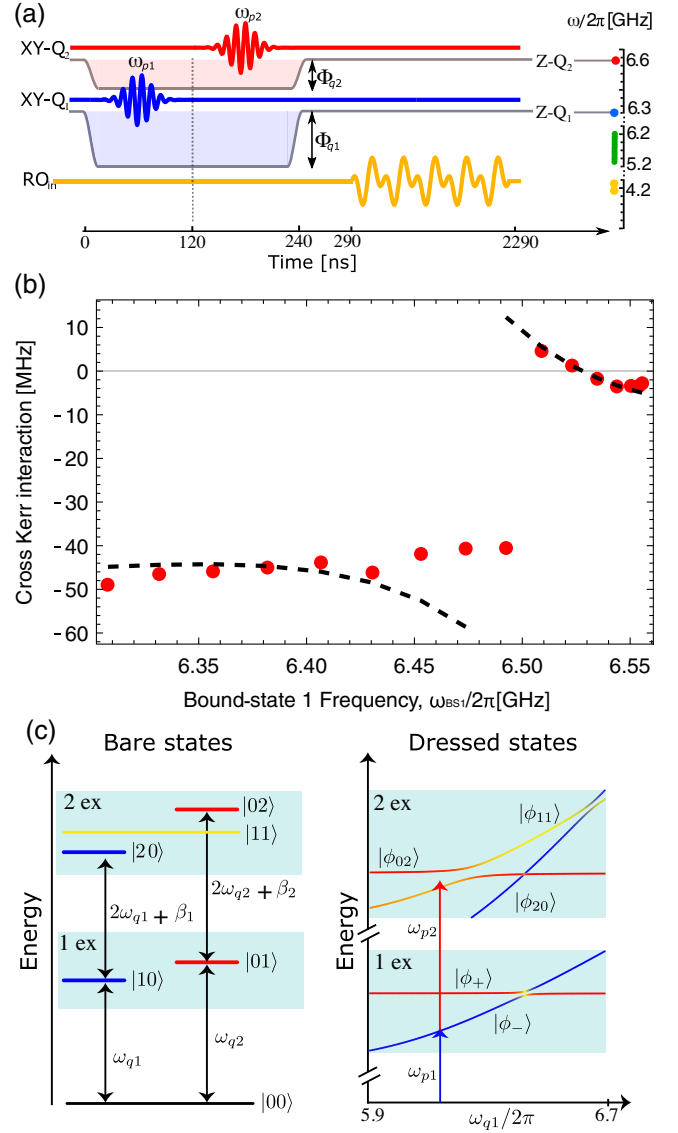

FIG. 8. Bound-state interaction in two-excitation subspace. (a) Pulse sequence. After tuning the bound-state frequency with flux pulses (red and blue shaded area), they are excited (red and blue lines) and their population is read out. (b) Cross-Kerr interaction and avoided crossing between the states $|02\rangle$ and $|11\rangle$ for the frequency of the Q_2 bound state $\omega_{\text{BS/2}}/2\pi = 6.653$ GHz. The dashed line represents the expected value calculated with the Hamiltonian Eq. (C1). (c) Energy-level scheme for the bare (left) and dressed (right) states.

simplified version of the complete energy structure of our system. In fact, the three photonic bands that originate from the coupled cavity array are not included in the figure (see Appendix B 5 for more details).

IV. DISCUSSION AND CONCLUSION

In summary, we introduced a new implementation of a finite-band waveguide made out of an array of high-impedance resonators to which we coupled two artificial

atoms. We measured the transmission spectrum of the coupled resonator array, highlighting the underlying multi-mode interactions with the artificial atom, and we observed the formation of the atom-photon bound states in the band gap. We demonstrated full control in accessing and preparing the atom-photon bound states in both the single- and double-excitation subspace. We characterized the resonant interaction between two bound states in the static and dynamic regimes, measuring an effective coupling strength up to 52 MHz and an excitation swap time down to 13 ns. Finally, we investigated the ZZ interaction between two detuned bound states, reaching a value up to 49 MHz. As shown in simulations, we expect a straightforward optimization of the device parameters to significantly improve our ability to control as well as suppress these interactions.

Compared to previous implementations of superconducting qubits coupled to gapped waveguides, our approach based on high-impedance resonators makes it possible to reach atom-cavity coupling strengths of a few hundred MHz while maintaining the resonators' footprint comparable to the one of the artificial atoms. Small footprints and strong interactions translate to a higher extensibility of our platform, with the foreseen possibility of adding more qubits as well as anchoring points to move towards two-dimensional lattices [47].

The tunable-range interactions between atom-photon bound states available in this platform find application to the quantum simulation of spin models [22]. At the same time, the possibility to implement fast and high-contrast SWAP and CZ gates using the array as a quantum bus could be further investigated in the context of quantum computing. From the perspective of quantum optics, this platform is amenable to studies of correlated nonlinear photon transport [14,48,49] and quantum nonlinear optics protocols [15]. By varying the coupling strength between neighboring sites, it is possible to engineer the band structure of the array and to endow it with nontrivial topological properties [34]. The intrinsic nonlinearity of the array, whose strength can be adjusted by design, could be utilized to implement recent theory proposals describing exotic light-matter interaction effects [50–52]. Finally, from the viewpoint of the fabrication, suspended junction arrays [53] may reduce their stray capacitance to ground. Additionally, from a material perspective, replacing Josephson-junction arrays with high-kinetic inductance superinductors [54–57] may lead to a more robust fabrication process and reduced disorder in the array.

APPENDIX A: EXPERIMENTAL DETAILS

1. Experimental setup

The complete experimental setup is shown in Fig. 9. The sample is wire bonded in a nonmagnetic oxygen-free copper sample box (see Appendix C 3), mounted to the mixing chamber stage of a dilution refrigerator operating at 10 mK and shielded by additional copper and μ-metal cans. Two additional shields (in order, copper and μ-metal) are placed around the sample in a light-tight fashion. The signal to the Q_1 and Q_2 charge lines (XY-Q_1 and XY-Q_2, respectively), to the waveguide (WG$_\text{in}$), and to readout resonators (RO$_\text{in}$) is delivered by highly attenuated coaxial lines (nominal total attenuation of -60 dB). The flux lines (Z-Q_1 and Z-Q_2) do not have any attenuation at the last two stages (total nominal attenuation -33 dB), but they are equipped with a 4-GHz low-pass filter for reducing flux noise from higher stages. The transmitted signals (through the couple cavity array and through the readout feedline) are amplified with a high electron mobility transistor (HEMT) amplifier at 3 K, further amplified at room temperature.

The microwave control for Q_1 (blue area) and Q_2 (red area) is achieved by up-converting the inphase (I) and the quadrature (Q) components of a low-frequency pulse generated by an arbitrary waveform generator (AWG), while the flux control is obtained by injecting current generated directly by two AWG channels. The qubit readout pulse is up- and down-converted with the same local oscillator (LO) (yellow area). Finally, the waveguide coherent spectroscopy is set up with a vector network analyzer (VNA) (green area).

2. State preparation of Q_1

Using the same pulse scheme as the one shown in Fig. 10(a) applied on Q_1, we measure its population as a
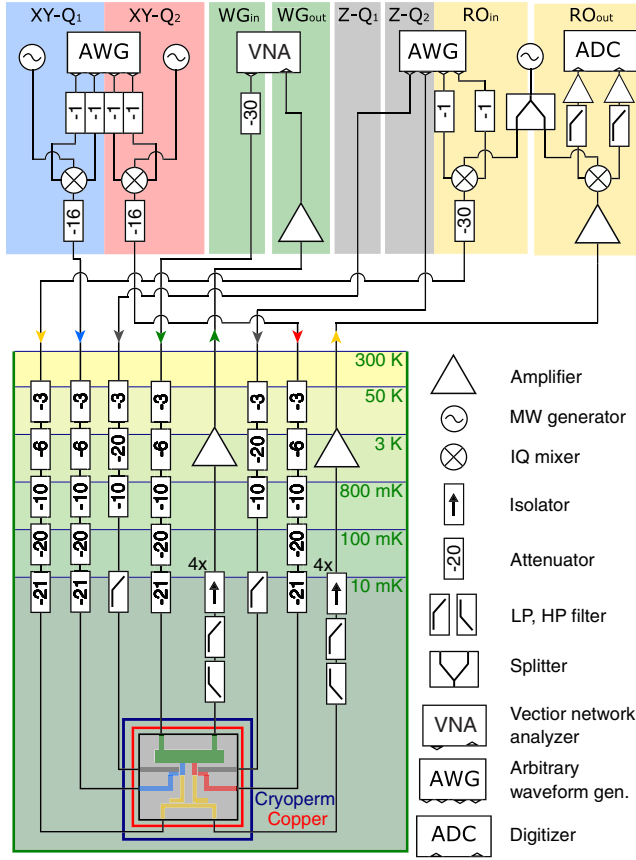
FIG. 9. Complete wiring diagram and room-temperature setup. The coherent tone to the waveguide is generated and measured with a vector network analyzer (VNA). The Q_1 and Q_2 driving (blue and red, respectively) are made by analog up-conversion of the pulse generated by an arbitrary waveform generator (AWG). The flux lines are controlled by two AWG channels. Finally, the qubit readout (yellow) is controlled by the up- and down-conversion of a pulsed generated by an AWG and logged by an analog-to-digital converter (ADC).

3. Photon number estimation

We calibrate the photon number in the array modes using the mode Kerr nonlinearity inherited by the Josephson-junction array resonators. The self-Kerr coefficient of the bare resonator scales with the inverse square of the number
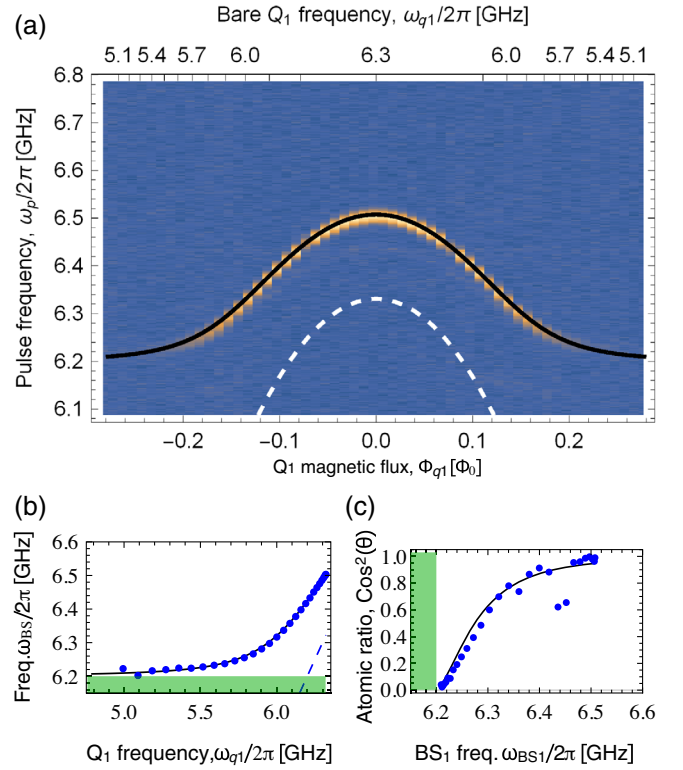

FIG. 10. State preparation of the isolated Q_1. (a) Population of Q_1 as a function of flux pulse amplitude Φ_{q1} and driving pulse frequency ω_p. The black line shows the fit of the bound-state energy given in Eq. (4) to the measured data. The white dashed line shows the bare Q_1 frequency calculated with the parameters extracted from the fit. (b) Bound-state frequency extracted from panel (a) as a function of the bare Q_1 frequency. (c) Atomic fraction of the excitation, extracted from the relative population measured in the qubit. The black line shows the expected value of the mixing angles as predicted from the ideal case theory given in Eq. (B24) using the parameters extracted from the fit in (a) and (b).

function of the bare qubit frequency (dashed white line) and driving pulse frequency ω_p. The result, reported in Fig. 10(a), shows the Q_1 largest frequency, $\omega_{q1,m} = 6.332$ GHz, smaller than Q_2 but compatible with the fabrication yields. The fit of the bound-state frequency given by Eq. (4) is in good agreement with the data (solid black line). The plot of the extracted $\omega_{BS,1}$ as a function of the bare qubit frequency is shown in Fig. 10(b), and the atomic population fraction is reported in Fig. 10(c), where the solid line is the calculated value with the parameters extracted from the fit.

of junctions, $K_r = e^2/(2 \times 10^2 \times C_r) = 2\pi \times 2.1$ MHz. Moreover, the nonlinearity is further diluted in each mode as with an effective Kerr, $K = K_r/N = 2\pi \times 100$ kHz; in fact, two excitations in one mode, in the momentum space, are spatially distributed to all the resonators of the array [58]. We can experimentally confirm this estimation by investigating the power response of the array modes.

Figure 11 shows the phase and magnitude of a coherent microwave tone in the range of mode number 8 at 5.552 GHz. Adapting the treatment in Ref. [59] to a transmission configuration and assuming a total input attenuation at the sample equal to 70 dB, we can globally fit the data to

$$S_{21} = \frac{\kappa}{\kappa_{\text{tot}}} \frac{1}{1/2 + i\delta + i\xi\tilde{n}}, \quad (A1)$$
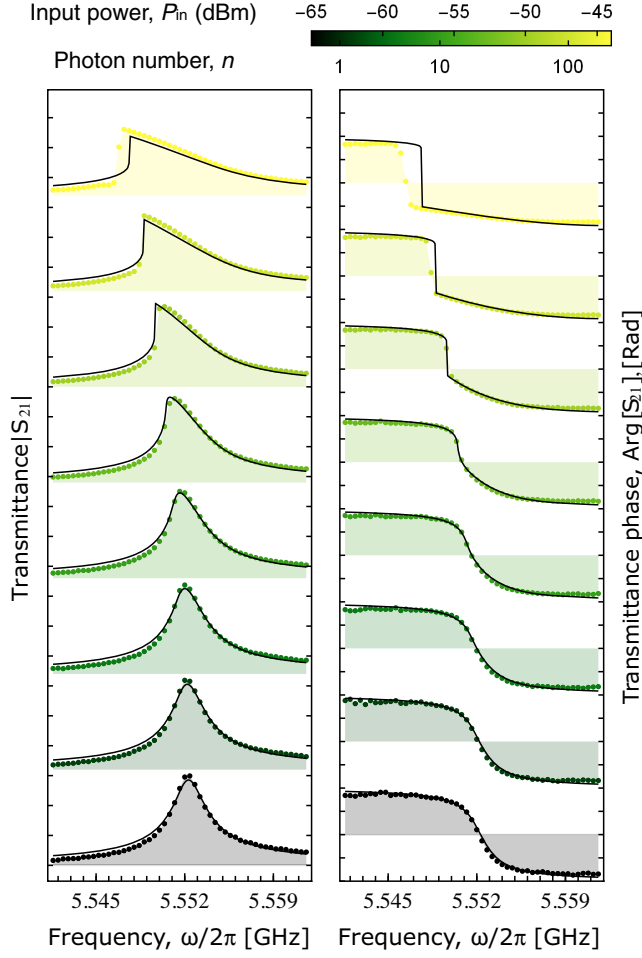
FIG. 11.   Single coherent tone spectroscopy of a single mode. (a) Magnitude and (b) phase of the transmission of the mode of the coupled-cavity array at 5.552 GHz as a function of power. The self-Kerr from the JJ array resonator is inherited by the modes. The coherent tone addresses only one cavity mode, so the global fit of a Kerr nonlinear resonator (solid line) is used to extract the self-Kerr K and the photon number n of the array mode. The shade areas indicate the deviation from zero transmission (deviation from the zero phase).

where κ is the external coupling rate, κ_{tot} is the total loss rate, $\delta = (\omega - \omega_0)/\kappa_{tot}$ is the relative detuning, $\xi = (P_{in}/\hbar\omega)\kappa K/\kappa_{tot}^3$ is the (adimensional) input power, K is the mode Kerr, and finally $\tilde{n}$ is given by the solution of the algebraic equation

$$1 = (\delta^2 + 1/4)\tilde{n} - 2\delta\xi\tilde{n}^2 + \xi^3\tilde{n}^3. \qquad \text{(A2)}$$

The global fit (solid black lines) reproduces the data well.

4. System parameters

The complete list of the system parameters measured in our sample is shown in Table I.

TABLE I.   Complete list of the system parameters.

Parameter	Value
Resonators	
Resonator capacitance, C_r	91.3 fF
Resonator inductance, L_r	8.87 nH
Resonator frequency, $\omega_r/2\pi$	5.593 GHz
Resonator impedance, Z_r	312 Ω
Nonradiative decay $\gamma_r/2\pi$	300 kHz
Resonator self-Kerr, $K_r/2\pi$	2.1 MHz
Coupled resonators array	
Passband center, $\omega_r'/2\pi$	5.717 GHz
Nearest-neighbor coupling, $J/2\pi$	249 MHz
Next-nearest-neighbor coupling, $J^{(2)}/2\pi$	38 MHz
Edges coupling $\kappa/2\pi$	12 MHz
Modes self-Kerr, $K/2\pi$	0.1 MHz
Lattice constant, d	200 μm
Band edge group index, $n_{g,e}$	Divergent
Band center group index, $n_{g,c}$	975
Qubits	
Q_1 maximum frequency $\omega_{q1,m}/2\pi$	6.322 GHz
Q_2 maximum frequency $\omega_{q2,m}/2\pi$	6.606 GHz
Q_1 anharmonicity $\beta_1/2\pi$	−266 MHz
Q_2 anharmonicity $\beta_2/2\pi$	−257 MHz
Q_1-array coupling $g_1/2\pi$	338 MHz
Q_2-array coupling $g_2/2\pi$	311 MHz
Nonradiative decay $\gamma_{q1,2}/2\pi$	≈50 kHz
Readout resonators	
RO-Q_1 frequency $\omega_{ro1}/2\pi$	4.280 GHz
RO-Q_2 frequency $\omega_{ro2}/2\pi$	4.412 GHz
RO-Q_1 coupling $h_1/2\pi$	98 ± 1 MHz
RO-Q_2 coupling $h_2/2\pi$	89 ± 1 MHz
Nonradiative decay $\gamma_c/2\pi$	≈50 kHz

APPENDIX B: THEORETICAL MODEL

1. Circuit model

The ideal circuit model of the system is sketched in Fig. 12 and shows N LC resonators, with capacitance C_r and inductance L_r, capacitively coupled in series via a
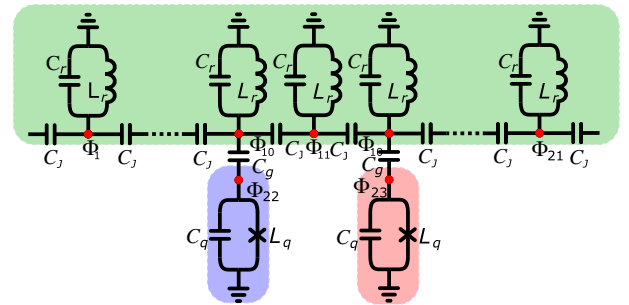

FIG. 12.   Circuit model for $N = 21$ capacitively coupled LC resonators (in green). The resonators at the edges of the array are capacitively coupled to a 50-Ω transmission line. Two transmon qubits are coupled at sites $x = 10$ (blue) and $x = 12$ (red).

capacitance C_J. Two sites of the array, $x_1 = 10$ and $x_2 = 12$, are coupled to two transmon qubits, represented by a Cooper pair box with capacitance C_q and Josephson energy E_J, via the coupling C_{gi}.

To start, we consider the bare coupled cavity array waveguide, whose unit cell has a lattice constant $d = 200\ \mu$m. For probing frequency ω that respects the homogeneity condition $d < \lambda_g/4$ for the electromagnetic waves, we can treat the coupled-cavity array as a composite right-left-handed transmission line.

Defining the lattice unit impedance $Z_l(\omega) = 1/i\omega C_J$ and admittance $Y_l(\omega) = (i\omega C_r + 1/i\omega L_r)$, we can follow standard procedures [60] to obtain the dispersion relation:

$$\cos(kd) = 1 + \frac{1}{2} Y_l Z_l. \tag{B1}$$

This equation can be recast in terms of the resonator frequency, $\omega_r = 1/\sqrt{\bar{C}_r L_r}$, with $\bar{C}_r = C_r + 2C_J$, in the limit of $C_J \ll \bar{C}_r$, and it reads

$$\omega = \omega_r + C_J Z_r \omega_r^2 \cos(kd), \tag{B2}$$

where $Z_r = \sqrt{L_r/\bar{C}_r}$ is the characteristic impedance of the resonator. From the dispersion relation Eq. (B1), we calculate the group velocity at the center of the band, $\omega = \omega_r$,

$$v_g(\omega_r) = C_J Z_r \omega_r^2 d, \tag{B3}$$

which gives us a left-handed dispersion with negative phase velocity [60]. Finally, we observe that the characteristic impedance of the transmission line is equal to

$$Z(\omega) = \sqrt{\frac{Z_l}{Y_l}} \approx \sqrt{\frac{L_r}{C_J}}\sqrt{\frac{1}{1 - (\frac{\omega}{\omega_r})^2}}. \tag{B4}$$

After having characterized the waveguide properties, we can take into consideration the full circuit model including the qubits. The Lagrangian of the circuit can be written in terms of the resonator and qubit fluxes, Φ_x and Φ_{qi}, respectively [61], and reads

$$\mathcal{L} = \frac{1}{2}\dot{\mathbf{\Phi}}^T \mathcal{C} \dot{\mathbf{\Phi}} - V, \tag{B5}$$

where $\dot{\mathbf{\Phi}}^T = (\dot{\Phi}_{q1}, \dot{\Phi}_{q2}, \dot{\Phi}_1, ..., \dot{\Phi}_N)$ and

$$V = \sum_x \frac{\Phi_x^2}{2L_x} - \sum_{i=1}^{2} E_J \cos\left(\frac{\Phi_{qi}}{\Phi_0}\right) \tag{B6}$$

is the potential energy term, with $\Phi_0 = h/(2e)$ being the flux quantum. The first term of Eq. (B5) is the kinetic term that is governed by the capacitance matrix

$$\mathcal{C} = \begin{pmatrix} \bar{C}_{q1} & 0 & 0 & 0 & \cdots & -C_{g1} & 0 & 0 & \cdots & 0 \\ 0 & \bar{C}_{q2} & 0 & 0 & & 0 & 0 & -C_{g2} & & 0 \\ 0 & 0 & \bar{C}_r & -C_J & & 0 & 0 & 0 & & 0 \\ 0 & 0 & -C_J & \bar{C}_r & \ddots & 0 & 0 & 0 & & 0 \\ \vdots & & & \ddots & \ddots & & & & & \vdots \\ -C_{g1} & 0 & 0 & 0 & & \bar{C}_r & -C_J & 0 & & 0 \\ 0 & 0 & 0 & 0 & & -C_J & \bar{C}_r & -C_J & & 0 \\ 0 & -C_{g2} & 0 & 0 & & 0 & -C_J & \bar{C}_r & \ddots & 0 \\ \vdots & & & & & & \ddots & \ddots & \ddots & -C_J \\ 0 & 0 & 0 & 0 & \cdots & 0 & 0 & 0 & -C_J & \bar{C}_r \end{pmatrix}, \tag{B7}$$

where $\bar{C}_{qi} = C_{qi} + C_{gi}$. The Hamiltonian of the system is obtained from the Lagrangian (B5) via the usual Legendre transformation [61] $H = \mathbf{Q}^T \dot{\mathbf{\Phi}} - \mathcal{L}$, where we introduced the conjugate charge variables $\mathbf{Q} = \partial\mathcal{L}/\partial\dot{\mathbf{\Phi}} = \mathcal{C}\dot{\mathbf{\Phi}}$, with $\mathbf{Q}^T = (Q_{q1}, Q_{q2}, Q_1, ..., Q_N)$. In the matrix notation, the Hamiltonian reads

$$H = \frac{1}{2}\mathbf{Q}^T \mathcal{C}^{-1}\mathbf{Q} + V, \tag{B8}$$

where now the coupling between the charges is governed by the inverse of the capacitance matrix $\mathcal{C}^{-1}$. In order to quantize the Hamiltonian Eq. (B8), we first express the

charge and the flux of the resonators in terms of the annihilation and creation operators:

$$Q_x = \sqrt{\hbar \bar{C}_r \omega_r / 2}(a^\dagger + a),$$

$$\Phi_x = i\sqrt{\hbar/(2\bar{C}_r \omega_r)}(a^\dagger - a). \qquad (B9)$$

In this way, the canonical commutation relations $[\Phi_x Q_{x'}] = i\hbar\delta_{x,x'}$ are satisfied.

The qubits can be described by nonlinear resonators with a Kerr nonlinearity β_i and annihilation (creation) operators b ($b^\dagger$). The qubit frequency is given by the frequency difference between the two lowest energy states, $|0\rangle$ and $|1\rangle$, of the transmon, and it is a function of the flux on the qubit, i.e., $\omega_{qi} = \omega_{qi}(\Phi_{qi})$. The transition between the first two transmon levels is determined by the dipole moment $D_{qi} = \langle 1|Q_{qi}|0\rangle$, and it defines the qubit-cavity couplings $g_i = D_{qi}\sqrt{\bar{C}_r\omega_r/(2\bar{C}_g^2)}$, where $(1/\bar{C}_{gi}) = (C_{gi}/\bar{C}_{qi}\bar{C}_r)$. Finally, with $(1/\bar{C}_J) = (C_J/\bar{C}_r^2)$, by defining the cavity-cavity hopping $J = \bar{C}_r\omega_r/(2\bar{C}_J)$, we obtain the system Hamiltonian given in Eq. (3). Note that in this derivation, we neglected direct parasitic capacitive couplings and disorder in the circuit elements, and we made some simplifications on the inverse capacitance matrix. We discuss the effect of these approximations in detail in Appendix C.

2. Bare coupled-cavity array in the tight-binding picture

Here, we rediscuss the bare array of coupled resonators starting from the standard tight-binding model with uniform nearest-neighbor couplings

$$H_{\text{CCA}} = \omega_r \sum_{x=1}^{N} a_x^\dagger a_x + J \sum_{x=1}^{N-1}(a_{x+1}^\dagger a_x + \text{H.c.}) \qquad (B10)$$

with ladder operators a_x fulfilling the usual bosonic commutation rules, $[a_x, a_{x'}^\dagger] = \delta_{x,x'}$. It is worth stressing that here N must be finite and the array subject to open boundary conditions, in contrast to most treatments in the literature of bound states, which focus on the thermodynamic limit and periodic boundary conditions.

The array's free Hamiltonian (B10) is diagonalized as (see, e.g., Ref. [62])

$$H_{\text{CCA}} = \sum_k \omega_k a_k^\dagger a_k, \qquad (B11)$$

with the normal modes a_k given by

$$a_k = \sqrt{\frac{2}{N+1}} \sum_{x=1}^{N} \sin(kx) a_x \qquad (B12)$$

and the normal frequencies ω_k by

$$\omega_k = \omega_r + 2J\cos k, \qquad (B13)$$

with

$$k = \frac{m\pi}{N+1} \quad (m = 1, 2, ..., N). \qquad (B14)$$

Note that the discrete spectrum (B13) obtained by a tight-binding array with open boundary conditions coincides with the one obtained by the circuit model in Eq. (B2).

3. One-atom bound states

Consider the case that only one atom is effectively coupled to the coupled-cavity array (the other being far detuned from the photonic band). Then, the total Hamiltonian Eq. (3), in terms of normal modes (B12) and in a frame rotating at frequency ω_r, reads (we omitted the label i in this case)

$$H = 2J\sum_k \cos k\, a_k^\dagger a_k + \delta b^\dagger b \qquad (B15)$$

$$+ g\sqrt{\frac{2}{N+1}} \sum_k \sin(kx_q)(a_k^\dagger b + a_k b^\dagger), \qquad (B16)$$

where $\delta = \omega_q - \omega_r$ is the detuning of the qubit from the bare frequency of each resonator and x_q the cavity to which the atom is directly coupled. Note the sine-shaped atom-mode interaction strength (colored coupling), stemming from the open boundary conditions to which the array is subject [63]. As shown next, such a colored coupling could generally lead to results slightly different from the usual white coupling under periodic boundary conditions [16–18,63].

Within the single-excitation subspace defined by $n = 1$, an atom-photon bound state $|\phi\rangle$ can be worked out as an eigenstate of the total Hamiltonian whose corresponding energy lies outside the photonic band, that is, such that $H|\phi\rangle = \hbar\omega|\phi\rangle$ with $|\omega| > 2J$. Expanding $|\phi\rangle$ in the basis $\{b^\dagger|g, 0\rangle, \{a_k^\dagger|g, 0\rangle\}\}$ as

$$|\phi\rangle = \left(c_q b^\dagger + \sum_k u_k a_k^\dagger\right)|g, 0\rangle \qquad (B17)$$

and then inserting this into the Schrödinger equation, we find that the frequency ω must fulfill the equation

$$\hbar(\omega - \delta) = \Sigma(\omega), \qquad (B18)$$

where the self-energy $\Sigma(\omega)$ is given by

$$\Sigma(\omega)/\hbar = \frac{2g^2}{N+1}\sum_k \frac{\sin^2\left(\frac{k}{2}x_q\right)}{\omega - 2J\cos\frac{k}{2}}$$

$$= \frac{g^2}{2J}\frac{1 - e^{-2\frac{x_q}{\lambda}} - e^{-2\frac{N+1-x_q}{\lambda}} + e^{-2\frac{N+1}{\lambda}}}{\sinh\left[\frac{1}{\lambda}\left(1 - e^{-2\frac{N+1}{\lambda}}\right)\right]} \quad (B19)$$

with

$$\lambda(\omega) = \left(\text{arccosh}\frac{|\omega|}{2J}\right)^{-1}. \quad (B20)$$

The solutions of Eq. (B18) with $|\omega| > 2J$ correspond to the atom-photon bound states. In the standard case of periodic boundary conditions, two bound states—one with energy above and one below the band—always exist [17,18]. In our case, however, the presence of array edges may affect the existence of bound states. By substituting in the eigenvalue Eq. (B18) the limiting values of the self-energy $\Sigma(\omega)$ for $\omega \to \pm 2J$, the condition for the existence of bound states is obtained as

$$g^2 > \frac{J(N+1)(2J \mp \delta)}{x_q(N+1-x_q)}, \quad (B21)$$

where $-\,(+)$ indicates a solution with energy above (below) the band. In our experimental setup, $g \sim J$, $N = 21$, and $x_q = 10, 12$ so that Eq. (B21) is always satisfied and the self-energy is well approximated by performing the thermodynamic limit

$$\Sigma(\omega)/\hbar \simeq \frac{g^2}{\omega\sqrt{1 - \frac{4J^2}{\omega^2}}}. \quad (B22)$$

In practice, this means that the atom in our setup is sufficiently far from the edges and that the number of resonators is large enough that the bound state can be calculated as if the array were infinitely long (in line with standard treatments).

Following Ref. [17], the bound state corresponding to a solution ω_{BS} can thus be worked out in the form

$$|\phi\rangle = [\cos\theta b^\dagger + (-1)^s \sin\theta \alpha^\dagger]|g, 0\rangle, \quad (B23)$$

where θ is given by

$$\cos\theta = \left(1 + \frac{g^2}{\omega_{\text{BS}}^2\left(1 - \frac{4J^2}{\omega_{\text{BS}}^2}\right)^{\frac{3}{2}}}\right)^{-\frac{1}{2}}, \quad (B24)$$

while

$$\alpha = \sum_x \frac{s^{|x-x_q|}e^{-\frac{|x-x_q|}{\lambda_\pm}}}{\sqrt{\coth\frac{1}{\lambda_\pm}}}a_x \quad (B25)$$

defines a bosonic ladder operator. Here, $\lambda = \lambda(\omega_{\text{BS}})$ as given by Eq. (B20), while $s = \text{sgn}(\omega_{\text{BS}})$ so that $s = +1$ when ω_{BS} lies above the band and $s = -1$ when it falls below.

The mixing angle θ measures the degree of hybridization: The dressed state is fully atomic for $\theta = 0$ and fully photonic for $\theta = \pi/2$. Equation (B25) fully defines the (normalized) photonic component, showing that the spatial mode is exponentially localized around the atom's position x_q. Accordingly, the parameter λ represents the localization length of the photonic cloud surrounding the atom.

4. Two-atom bound states

Let us now study the case of bound states in the single-excitation sector when two atoms are coupled to resonators x_1 and x_2, respectively. The total Hamiltonian is the natural generalization of Eq. (B15), and it now features the detuning of each qubit $\delta_i = \omega_{qi} - \omega_r$ and the corresponding coupling strength g_i with $i = 1, 2$.

In this case, an effective interaction between bound states arises when the photonic clouds of the individual bound states overlap. This interaction changes the bound-state energies, which are now given by the real solutions with $|\omega| > 2J$ of the transcendental equation [17]

$$(\omega - \delta_1 - \Sigma_1)(\omega - \delta_2 - \Sigma_2) = \Sigma_1\Sigma_2 e^{-2\frac{|x_1-x_2|}{\lambda}}. \quad (B26)$$

Here, Σ_i is the self-energy of the ith qubit (in the absence of the other qubit) as given by Eq. (B22) for $g = g_i$.

Equation (B26) admits up to four real solutions (and as many bound states). Based on the performed measurements in our experiment, we focus on the case of bound-state energies above the band. Then, the pair of bound states with energies $\omega_\pm$ are given by

$$|\phi_\pm\rangle = \frac{1}{\sqrt{1 + |\xi|^2}}[D_\pm^\dagger(x_1) \pm \xi D_\pm^\dagger(x_2)]|g_1, g_2, 0\rangle, \quad (B27)$$

where we defined the dressed ladder operators

$$D_\pm(x_i) = \cos(\theta_\pm)b_i + \sin(\theta_\pm)\frac{1}{\mathcal{N}_\pm}\sum_x e^{-\frac{|x-x_i|}{\lambda_\pm}}a_x \quad (B28)$$

and the mixing angle

$$\cos\theta_\pm = \left(1 + \frac{g_1 g_2 \mathcal{N}_\pm^2}{4J^2\sinh^2\frac{1}{\lambda_\pm}}\right)^{-\frac{1}{2}}, \quad (B29)$$

with

$$\mathcal{N}_\pm = \sqrt{\coth\frac{1}{\lambda_\pm}\left(1 \pm e^{-\frac{|x_1-x_2|}{\lambda_\pm}}\right) \pm |x_1 - x_2|e^{-\frac{|x_1-x_2|}{\lambda_\pm}}}.$$

The parameter $\xi = \xi(\omega_\pm)$ gives the amount of the hybridization between the two atoms and reads

$$\xi(\omega_\pm) = \frac{\sqrt{\Sigma_1 \Sigma_2} e^{-\frac{|x_1 - x_2|}{\lambda}}}{\omega_\pm - \delta_2 - \Sigma_2}. \tag{B30}$$

In the regime of equal coupling $g_1 = g_2$ (quite close to our experimental realization) and in correspondence with the avoided crossing, $\delta_1 = \delta_2$, the two bound states get completely hybridized, $\xi(\omega_\pm) = 1$, and the labels $+(-)$ signify the bound states with even (odd) symmetry with respect to the atoms' midpoint.

Under certain conditions, the interaction can push the odd-parity bound-state frequency into the propagating band (in which case the state no longer exists). Similarly to Eq. (B21), an existence condition for this antisymmetric state can be worked out by taking the limit $\omega \to 2J^+$ in Eq. (B26), which yields (for $g_1 = g_2 = g$)

$$g^2 > \frac{J(4J - \delta_1 - \delta_2)}{|x_1 - x_2|}. \tag{B31}$$

The melting of this bound state into the photonic band reported in Fig. 6 indeed occurs for parameters such that Eq. (B31) is not satisfied.

The interaction between one-atom bound states can also cause a (coherent) excitation transfer between the two atoms described by an effective spin Hamiltonian (the field is adiabatically eliminated). This occurs in the dispersive regime where the qubits are far detuned from the band edge, i.e., $\omega_{qi} - \omega_r - 2J \gg g_i$, and $\cos\theta_\pm \approx 1$ such that the bound states are mostly atomic. The effective spin Hamiltonian then reads [22,64]

$$H_{\text{eff}}/\hbar = \frac{g_1 g_2}{\delta_e} \sum_{ij=1}^{2} e^{-\frac{|x_i - x_j|}{\lambda}} b_i^\dagger b_j, \tag{B32}$$

where we assume that the atoms are tuned on resonance with one another, i.e., $\omega_{q1} = \omega_{q2} = \omega_q$, and set $\delta_e = \omega_q - \omega_r - 2J$ (detuning from the band edge). This Hamiltonian captures the excitation exchange dynamics between the qubits in Fig. 7. The coherence time is just given by the single-atom bound-state decay into the waveguide and into the other dissipation channels as discussed in the main text.

5. Two-photon bound states

We next study the energy of two-excitation bound states. In the ideal case $\beta \to -\infty$ (ideal two-level atom case), two-photon bound states are known to occur, entailing strong nonlinear effects [17,18]. Yet, even for finite β, the nonlinear energy spacing of levels above the first two can still affect two-excitation bound states, causing measurable deviations from the fully linear case $\beta = 0$ (as discussed in the main text). To show this in more detail, we first note that any state in the two-excitation sector can be written as
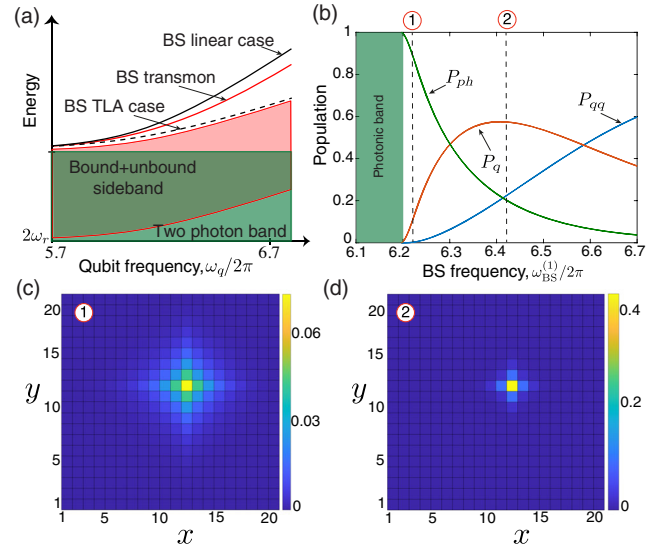

FIG. 13. (a) Sketch of the two-excitation spectrum (upper part) for a single qubit as a function of the qubit frequency. The bound states in the case of a linear resonator (black solid line) and an ideal two-level qubit (black dashed lines) are also shown for comparison (see main text for more details). (b) Excitation distribution of the two-photon bound state as a function of the single-excitation bound-state frequency. Specifically, we plot the probability of finding one or two excitations on the transmon, respectively given by $P_q = \sum_{x=1}^{N} |c_2(x)|^2$ and $P_{qq} = |c_{22}|^2$, along with the two-photon population $P_{ph} = \sum_{x=1}^{N} \sum_{y=1}^{N} |u(x,y)|^2$. (c,d) Spatial profile of the normalized two-photon wave function for the frequencies highlighted by the dashed vertical line in panel (b). The considered parameters are those corresponding to Q_2 (see Table I), with $\omega_r/2\pi = 5.7$ GHz, $J/2\pi = 249$ MHz, $g_2/2\pi = 311$ MHz, and $\beta_2/2\pi = -257$ MHz for the transmon qubit.

$$|\phi^{(2)}\rangle = \left(\frac{1}{\sqrt{2}} \sum_{i,j=1}^{2} c_{ij} b_i^\dagger b_j^\dagger + \sum_{i=1}^{2} \sum_x c_i(x) b_i^\dagger a_x^\dagger \right.$$
$$\left. + \frac{1}{\sqrt{2}} \sum_{x,y} u(x,y) a_x^\dagger a_y^\dagger \right) |g,0\rangle. \tag{B33}$$

Here, c_{ij} is the probability amplitude of having one excitation on transmon i and one on transmon j (including the case $i = j$), while $c_i(x)$ is the probability amplitude corresponding to one excitation on the ith transmon and another one in the waveguide. Finally, $u(x,y) = u(y,x)$ is the symmetric wave function of the two-photon bound-state component. By plugging Eq. (B33) into the Schrödinger equation generated by Hamiltonian Eq. (3), we numerically solve the resulting set of coupled equations.

In the following, we separately address the one- and two-atom cases.

a. One atom

Figure 13(a) shows the upper part of the two-excitation spectrum, $\omega > 2\omega_r$, as a function of the atom frequency.

The full spectrum (of which only the upper part is shown) features a band of two-photon unbound states defined by $\omega \in [2(\omega_r - 2J), 2(\omega_r + 2J)]$ plus a pair of sidebands $\omega \in [\omega_{\mathrm{BS}}^{(1)} - 2J, \omega_{\mathrm{BS}}^{(1)} + 2J]$, where $\omega_{\mathrm{BS}}^{(1)}$ is the energy of the single-excitation bound states. Additionally, there exists a pair of two-photon bound states (see Sec. II C 2) with discrete energies $\omega_{\mathrm{BS}}^{(2)}$ such that $|\omega_{\mathrm{BS}}^{(2)} - \omega_r| > 4J$ (one above and one below the continuous bands). For comparison, we also plot the bound-state energies in the limiting cases of a linear resonator (black solid line) and a two-level atom (black dashed line). In Fig. 5 of the main text, we defined the dressed-state anharmonicity as the difference in the bound-state energy between the linear and nonlinear cases. While Fig. 13(a) shows the occurrence of a two-excitation bound state, it is natural to wonder how hybridized such a state is, and additionally, if it features a significant two-photon component (or alternatively, if it is mostly populated by the excitation of the second transmon level). To clarify this point, in Fig. 13(b), we plot the population distribution of the two-excitation bound state, which clearly shows the photon dressed nature of the bound state in the considered parameter regime. Notably, the two-photon wave function exhibits a different localization length depending on the qubit frequency, in this respect similarly to the single-excitation case [see Figs. 13(c) and 13(d)].

b. Two atoms

As discussed in the main text, the two-excitation spectrum in the case of two atoms becomes quite involved, as shown in Fig. 14. Besides the two-photon unbound states with energies $\omega \in [2(\omega_r - 2J), 2(\omega_r + 2J)]$ (green box), two sidebands occur (above the main band) with energies
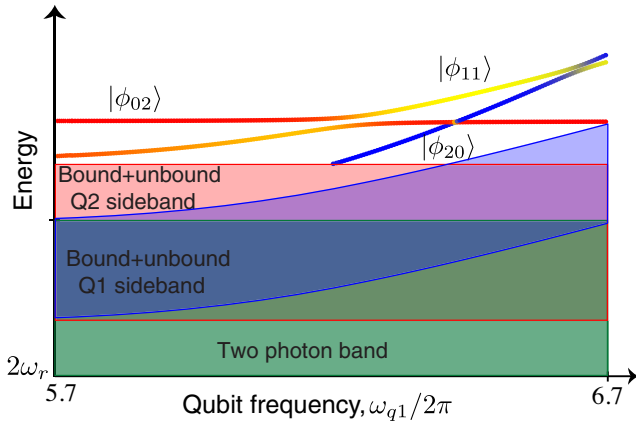

FIG. 14. Sketch of the two-excitation spectrum (upper part) as a function of the Q_1 frequency in the case of two qubits. We set the frequency of Q_2 to $\omega_{q2}/2\pi = 6.45$ GHz with the remaining parameters fixed to $\omega_r/2\pi = 5.7$ GHz, $J/2\pi = 249$ MHz, $g_2/2\pi = 311$ MHz, $g_1/2\pi = 338$ MHz, $\beta_2/2\pi = -257$ MHz, and $\beta_1/2\pi = -266$ MHz. In this way, the bound states correspond to the one shown in Fig. 8.

$\omega \in [\omega_+^{(1)} - 2J, \omega_+^{(1)} + 2J]$ and $\omega \in [\omega_-^{(1)} - 2J, \omega_-^{(1)} + 2J]$, where the $\pm$ sign refers to the two-atom single-excitation bound state discussed in Appendix B 4. Above the bands, there appear three bound states stemming from the hybridization of the bare qubit states $|20\rangle, |02\rangle$, and $|11\rangle$. Once coupled to the array, the transmons get highly hybridized both with one another and with the array field, resulting in the dressed states $|\phi_{20}\rangle, |\phi_{02}\rangle$, and $|\phi_{11}\rangle$ (the labels reflect the resemblance of each dressed state to the bare state of corresponding indices away from the avoided crossings). In particular, the color scale used in Fig. 14 reflects the population distribution among the two qubits, ranging from blue (excitation on Q_1) to red (Q_2).

6. Array transmission

We calculate the transmission through the array by applying the input-output theory relation to the Heisenberg equation [65]. The intracavity field a_x for the xth resonator and b_m for the mth qubit, with a driving field $a_{\mathrm{in}}(t) = a_{\mathrm{in}}e^{-i\omega t}$ applied on resonator $x = 1$, obey the differential equations

$$\dot{a}_x(t) = i[H, a_x(t)] - \frac{1}{2}\kappa a_x(t) + \sqrt{\kappa_r}\delta_{x1}a_{\mathrm{in}}, \quad (\text{B34})$$

$$\dot{b}_m(t) = i[H, b_i(t)] - \frac{1}{2}\gamma b_m(t), \quad (\text{B35})$$

where $\kappa = \delta_{x1}\kappa_r + \delta_{x21}\kappa_r + \kappa_{\mathrm{nr}}$ is the sum of radiative (in the case of the edge cavities) and nonradiative decay rates for the resonators, γ is the decay rate for the qubits, and H is the Hamiltonian in Eq. (3). In the steady state, $a_x(t) = e^{-i\omega t}a_x$, and the equations for the resonator and qubit fields become

$$0 = \left(\Delta_r - \frac{i}{2}\kappa\right)a_x + J(a_{x+1} + a_{x-1})$$
$$+ \delta_{xm}gb_m + i\sqrt{\kappa_r}\delta_{x1}a_{\mathrm{in}}, \quad (\text{B36})$$

$$0 = \left(\Delta_m + \frac{i}{2}\gamma\right)b_m + \delta_{xm}ga_x, \quad (\text{B37})$$

where we defined the tuning $\Delta_r = \omega_r - \omega$ and $\Delta_m = \omega_{qi} - \omega$. Solving the algebraic system and applying the input-output relation $\langle a_{\mathrm{out}}\rangle + \langle a_{\mathrm{in}}\rangle = \sqrt{\kappa_{\mathrm{nr}}}\langle a_x\rangle$, we calculate the transmission coefficient from cavity 1 to 21.

APPENDIX C: EXPERIMENTAL IMPERFECTIONS

1. Parasitic capacitance

As observed in the main text, the frequency distribution of the coupled-cavity array modes and the bound-state interaction strength cannot be quantitatively reproduced by neglecting capacitive couplings beyond the nearest neighbor.

Solving Poisson's equation with a finite element method solver (Comsol Multiphysics, electrostatic package), we

estimate a parasitic capacitance between next-nearest-neighbor resonators $C_J^{(2)} \approx 0.52$ fF and the one between qubits and resonator $C_g^{(2)} \approx 0.73$ fF. Adding this contribution to the capacitance matrix $\mathcal{C}$, with the definitions $(1/\bar{C}_J^{(2)}) = (C_J^{(2)}/\bar{C}_r^2)$ and $(1/\bar{C}_{gi}^{(2)}) = (C_{gi}^{(2)}/\bar{C}_r C_{qi}) + (C_r/\bar{C}_{qi}\bar{C}_J)$, it is finally possible to write the Hamiltonian:

$$
\begin{aligned}
H/\hbar = &\sum_{x=1}^{N} \omega_r a_x^\dagger a_x + \sum_{x=1}^{N-1} J(a_x^\dagger a_{x+1} + a_{x+1}^\dagger a_x) \\
&+ J^{(2)} \sum_{x=1}^{N-2} (a_{x+2}^\dagger a_x + \text{H.c.}) \\
&+ \sum_{i=1}^{2} \omega_{qi} b_i^\dagger a_i + \frac{1}{2}\beta_i b_i^\dagger b_i^\dagger b_i b_i + g_i(a_{x_i}^\dagger b_i + b_i^\dagger a_{x_i}) \\
&+ \sum_{i=1}^{2} g_i^{(2)}(a_{x_i+1}^\dagger b_i + b_i^\dagger a_{x_i+1} + a_{x_i-1}^\dagger b_i + b_i^\dagger a_{x_i-1}),
\end{aligned}
$$

(C1)

where we introduced the next-nearest-neighbor couplings $g_i^{(2)} = D_{qi}\sqrt{\bar{C}_r \omega_r / [2(\bar{C}_{gi}^{(2)})^2]}$ and $J^{(2)} = \omega_r \bar{C}_r / (2\bar{C}_J^{(2)})$.

2. Interaction strength optimization

In Fig. 15, we report the interaction strength of different designs based on the values of the device studied in this work. In particular, we calculate the expected bound-state interaction for the same parameters of the current sample, but we increase the free sites between the coupling points of the qubits. In the new configuration, the qubits are coupled to cavities 9 and 13, instead of 10 and 12. The same calculation is repeated, but we reduce the qubit-cavity
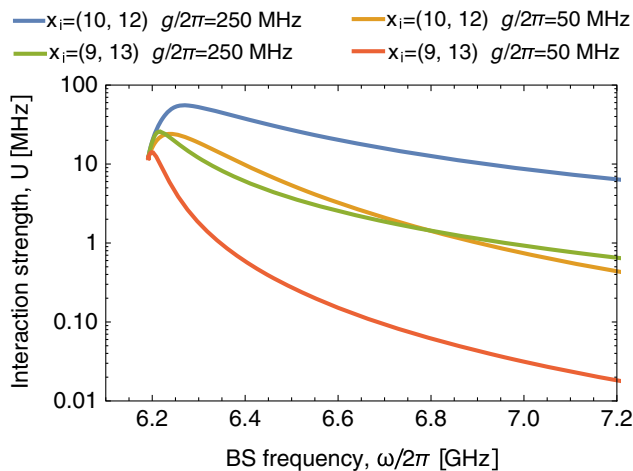

FIG. 15. Interaction strength between two bound states. The four lines represent the calculated coupling between two bound states, for qubits coupled to different array sites(x_i) and with different qubit-cavity coupling strengths g.

coupling to 50 MHz. With the latter configuration, we expect an on-off ratio of 1000 within a detuning range of 1 GHz.

3. Electromagnetic cross-talk

Four features of the transmission spectrum across the coupled-cavity array cannot be quantitatively explained by the ideal case. The transmitted signal reported in Fig. 16(c) (compare with Fig. 2 plotted with a linear scale) highlights the nonvanishing transmission outside the band, the "pairing" effect of modes, the transmission minima within the band, and finally the asymmetric mode distribution. These nonidealities are due to the non-negligible cross-talk between the input and output ports of the sample box and the next-nearest-neighbor interaction discussed in Appendix C 1.

Figure 1(a) reports a micrograph of the sample bonded to its sample holder. The bond wires connecting the sample box ports to the signal launcher on chip are approximately 1.5 mm long. We model their electromagnetic cross-talk as two power dividers, the first of which separates the incoming signal S_{in} into a part that reaches the second power divider after an electrical delay $e^{i\theta}$ and a part through the coupled-cavity array, $\varepsilon S_{\text{in}}$. In our model, the two signals are then recombined by the second power divider.

The solid line in Fig. 16(c) shows the prediction for our model with the fitting parameters $\varepsilon = 0.22$ and $\theta = 0.34\pi$. In comparison with a pure tight-binding model represented by the dashed black line, we can reproduce the main features of the transmission spectrum. Unfortunately, the mode distribution is still not completely described by the model. We attribute this behavior to fabrication imperfection, mainly on the smallest resonator feature represented by the junctions in the resonators. The design of the JJ resonator intrinsically mitigates the possible variance by a factor of $\sqrt{10}$. Moreover, although the individual modes are affected by this imperfection, the collective behavior of the coupled-cavity array as a waveguide is still close to ideal because of the large resonator-resonator coupling J.

We would like to stress that the cross-talk affects only the measured transmitted field and not the intrinsic mode structure.

4. Magnetic cross-talk

The flux lines Z-Q_1 and Z-Q_2 have a linear magnetic cross-talk that has been calibrated and compensated. The flux reported here is therefore the net flux in each SQUID loop and not the one produced by the aforementioned flux lines.

The relation between the flux in each SQUID, Φ_{q1} and Φ_{q2}, and the room-temperature voltages applied to the coaxial cable, V_1 and V_2, respectively, is expressed by

$$
\begin{pmatrix} \Phi_1 \\ \Phi_2 \end{pmatrix} = \begin{pmatrix} L_{11} & L_{12} \\ L_{21} & L_{22} \end{pmatrix} \begin{pmatrix} V_1 \\ V_2 \end{pmatrix} + \begin{pmatrix} \Phi_1^{\text{off}} \\ \Phi_2^{\text{off}} \end{pmatrix}, \quad \text{(C2)}
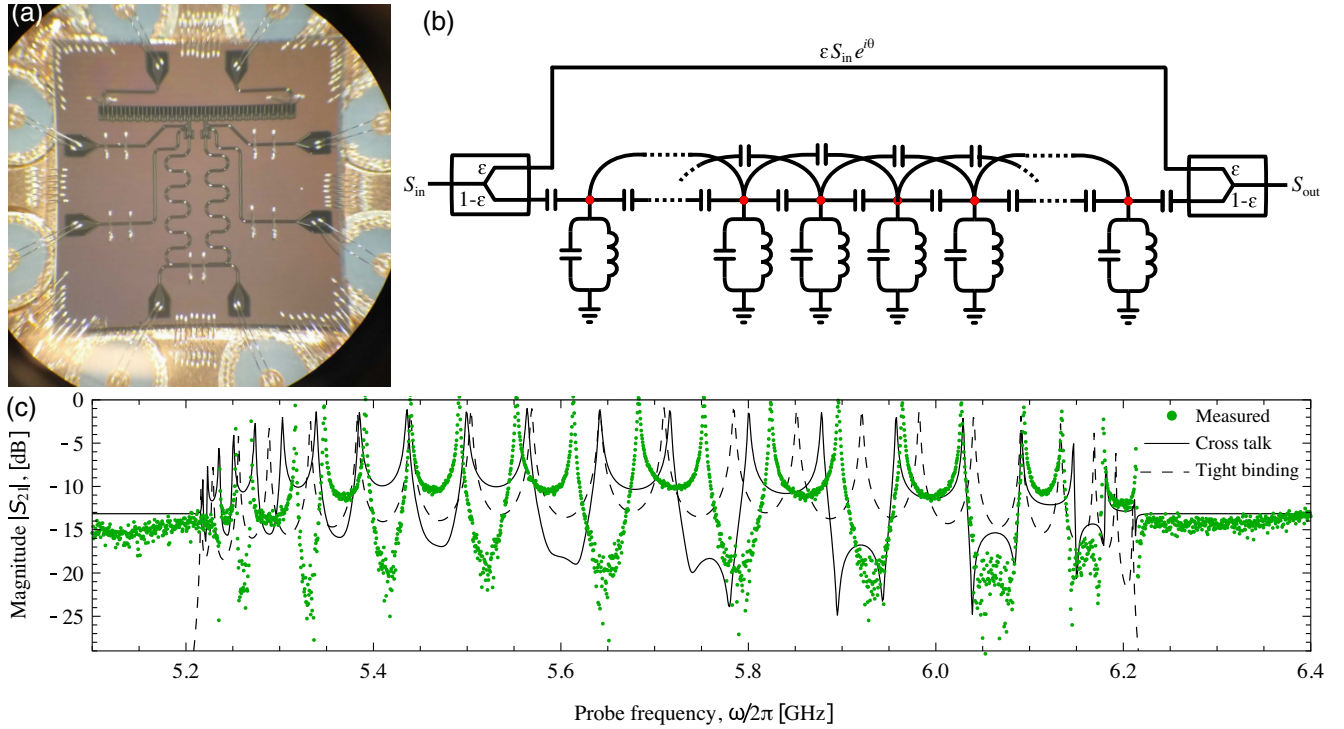$$

FIG. 16.   Transmission cross-talk. (a) Micrograph of the sample bonded in the copper sample box. The 1.5-mm aluminium bond wires connecting the inner conductor of a coaxial cable to the bond pad on the chips have direct electromagnetic cross-talk. (b) Model of the cross-talk consisting in two power splitters/combiners: A small portion of the signal bypasses the waveguide and is recollected at the output, constructively or destructively interfering with the signal through the waveguide, and producing a nonzero transmission outside the band. (c) Measured transmission through the sample (green dots), which is not well reproduced considering only the ideal case (input-output theory at low power, red dashed line). The sum on the signal through the array and the cross-talk (black solid line) explain the nonzero transmission and the "pairing" effect.

where we introduced the inductance matrix for the flux lines $\mathbf{L}_{\mathrm{fl}}$. From the measurement of the periodicity of the readout resonator of each qubit at different fluxes, we can extract the coefficients of the inductance matrix and the flux offset in each SQUID loop.

In order to decouple the two flux lines, we can redefine the voltages in each of them as

$$\begin{pmatrix} V_1 \\ V_2 \end{pmatrix} = \begin{pmatrix} L_{11} & L_{12} \\ L_{21} & L_{22} \end{pmatrix}^{-1} \begin{pmatrix} \Phi_1 - \Phi_1^{\mathrm{off}} \\ \Phi_2 - \Phi_2^{\mathrm{off}} \end{pmatrix}. \quad (\mathrm{C3})$$

For our sample, we measure an offset $\Phi_1^{\mathrm{off}}/\Phi_0 = 0.091$ and $\Phi_2^{\mathrm{off}}/\Phi_0 = 0.084$, while the relative magnetic cross-talk for Q_1 is $L_{12}/L_{11} = 0.041$ and for Q_2 it is $L_{21}/L_{22} = 0.063$.

[1] D. Roy, C. M. Wilson, and O. Firstenberg, *Colloquium: Strongly Interacting Photons in One-Dimensional Continuum*, Phys. Rev. Mod. Phys. **89**, 021001 (2017).

[2] P. Lodahl, S. Mahmoodian, S. Stobbe, A. Rauschenbeutel, P. Schneeweiss, J. Volz, H. Pichler, and P. Zoller, *Chiral Quantum Optics*, Nature (London) **541**, 473 (2017).

[3] H. Zheng, D. J. Gauthier, and H. U. Baranger, *Waveguide-QED-Based Photonic Quantum Computation*, Phys. Rev. Lett. **111**, 090502 (2013).

[4] V. Paulisch, H. J. Kimble, and A. González-Tudela, *Universal Quantum Computation in Waveguide QED Using Decoherence Free Subspaces*, New J. Phys. **18**, 043041 (2016).

[5] H. Pichler, S. Choi, P. Zoller, and M. D. Lukin, *Universal Photonic Quantum Computation via Time-Delayed Feedback*, Proc. Natl. Acad. Sci. U.S.A. **114**, 11362 (2017).

[6] J. Borregaard, A. S. Sørensen, and P. Lodahl, *Quantum Networks with Deterministic Spin–Photon Interfaces*, Adv. Quantum Techn. **2**, 1800091 (2019).

[7] I. Carusotto and C. Ciuti, *Quantum Fluids of Light*, Rev. Mod. Phys. **85**, 299 (2013).

[8] C. Noh and D. G. Angelakis, *Quantum Simulations and Many-Body Physics with Light*, Rep. Prog. Phys. **80**, 016401 (2017).

[9] D. E. Chang, J. S. Douglas, A. González-Tudela, C.-L. Hung, and H. J. Kimble, *Colloquium: Quantum Matter Built from Nanoscopic Lattices of Atoms and Photons*, Rev. Mod. Phys. **90**, 031002 (2018).

[10] A. S. Sheremet, M. I. Petrov, I. V. Iorsh, A. V. Poshakinskiy, and A. N. Poddubny, *Waveguide Quantum Electrodynamics: Collective Radiance and Photon-Photon Correlations*, arXiv:2103.06824.

[11] V. P. Bykov, *Spontaneous Emission from a Medium With a Band Spectrum.*, Sov. J. Quantum Electron. **4**, 861 (1975).

[12] S. John and J. Wang, *Quantum Electrodynamics Near a Photonic Band Gap: Photon Bound States and Dressed Atoms*, Phys. Rev. Lett. **64**, 2418 (1990).

[13] S. John and T. Quang, *Spontaneous Emission Near the Edge of a Photonic Band Gap*, Phys. Rev. A **50**, 1764 (1994).

[14] P. Longo, P. Schmitteckert, and K. Busch, *Few-Photon Transport in Low-Dimensional Systems: Interaction-Induced Radiation Trapping*, Phys. Rev. Lett. **104**, 023602 (2010).

[15] D. E. Chang, V. Vuletić, and M. D. Lukin, *Quantum Nonlinear Optics—Photon by Photon*, Nat. Photonics **8**, 685 (2014).

[16] F. Lombardo, F. Ciccarello, and G. M. Palma, *Photon Localization versus Population Trapping in a Coupled-Cavity Array*, Phys. Rev. A **89**, 053826 (2014).

[17] G. Calajó, F. Ciccarello, D. Chang, and P. Rabl, *Atom-Field Dressed States in Slow-Light Waveguide QED*, Phys. Rev. A **93**, 033833 (2016).

[18] T. Shi, Y.-H. Wu, A. González-Tudela, and J. I. Cirac, *Bound States in Boson Impurity Models*, Phys. Rev. X **6**, 021027 (2016).

[19] E. Sánchez-Burillo, L. Martín-Moreno, J. J. García-Ripoll, and D. Zueco, *Single Photons by Quenching the Vacuum*, Phys. Rev. Lett. **123**, 013601 (2019).

[20] M. Bello, G. Platero, J. I. Cirac, and A. González-Tudela, *Unconventional Quantum Optics in Topological Waveguide QED*, Sci. Adv. **5**, 7 (2019).

[21] L. Leonforte, A. Carollo, and F. Ciccarello, *Vacancy-Like Dressed States in Topological Waveguide QED*, Phys. Rev. Lett. **126**, 063601 (2021).

[22] J. S. Douglas, H. Habibian, C. L. Hung, A. V. Gorshkov, H. J. Kimble, and D. E. Chang, *Quantum Many-Body Models with Cold Atoms Coupled to Photonic Crystals*, Nat. Photonics **9**, 326 (2015).

[23] A. González-Tudela, C.-L. Hung, D. E. Chang, J. I. Cirac, and H. Kimble, *Subwavelength Vacuum Lattices and Atom–Atom Interactions in Two-Dimensional Photonic Crystals*, Nat. Photonics **9**, 320 (2015).

[24] M. T. Manzoni, L. Mathey, and D. E. Chang, *Designing Exotic Many-Body States of Atomic Spin and Motion in Photonic Crystals*, Nat. Commun. **8**, 1 (2017).

[25] T. Shi, Y.-H. Wu, A. González-Tudela, and J. I. Cirac, *Effective Many-Body Hamiltonians of Qubit-Photon Bound States*, New J. Phys. **20**, 105005 (2018).

[26] R. K. Naik, N. Leung, S. Chakram, P. Groszkowski, Y. Lu, N. Earnest, D. C. McKay, J. Koch, and D. I. Schuster, *Random Access Quantum Information Processors*, Nat. Commun. **8**, 1904 (2017).

[27] J. D. Hood, A. Goban, A. Asenjo-Garcia, M. Lu, S.-P. Yu, E. Chang, and H. J. Kimble, *Atom–Atom Interactions around the Band Edge of a Photonic Crystal Waveguide*, Proc. Natl. Acad. Sci. U.S.A. **113**, 10507 (2016).

[28] L. Krinner, M. Stewart, A. Pazmiño, J. Kwon, and D. Schneble, *Spontaneous Emission of Matter Waves from a Tunable Open Quantum System*, Nature (London) **559**, 589 (2018).

[29] M. Stewart, J. Kwon, A. Lanuza, and D. Schneble, *Dynamics of Matter-Wave Quantum Emitters in a Structured Vacuum*, Phys. Rev. Research **2**, 043307 (2020).

[30] Y. Liu and A. A. Houck, *Quantum Electrodynamics Near a Photonic Bandgap*, Nat. Phys. **13**, 48 (2017).

[31] N. M. Sundaresan, R. Lundgren, G. Zhu, A. V. Gorshkov, and A. A. Houck, *Interacting Qubit-Photon Bound States with Superconducting Circuits*, Phys. Rev. X **9**, 011021 (2019).

[32] M. Mirhosseini, E. Kim, V. S. Ferreira, M. Kalaee, A. Sipahigil, A. J. Keller, and O. Painter, *Superconducting Metamaterials for Waveguide Quantum Electrodynamics*, Nat. Commun. **9**, 3706 (2018).

[33] V. S. Ferreira, J. Banker, A. Sipahigil, M. H. Matheny, A. J. Keller, E. Kim, M. Mirhosseini, and O. Painter, *Collapse and Revival of an Artificial Atom Coupled to a Structured Photonic Reservoir*, arXiv:2001.03240.

[34] E. Kim, X. Zhang, V. S. Ferreira, J. Banker, J. K. Iverson, A. Sipahigil, M. Bello, A. González-Tudela, M. Mirhosseini, and O. Painter, *Quantum Electrodynamics in a Topological Waveguide*, Phys. Rev. X **11**, 011015 (2021).

[35] V. E. Manucharyan, J. Koch, L. I. Glazman, and M. H. Devoret, *Fluxonium: Single Cooper-Pair Circuit Free of Charge Offsets*, Science **326**, 113 (2009).

[36] N. A. Masluk, I. M. Pop, A. Kamal, Z. K. Minev, and M. H. Devoret, *Microwave Characterization of Josephson Junction Arrays: Implementing a Low Loss Superinductance*, Phys. Rev. Lett. **109**, 137002 (2012).

[37] M. T. Bell, I. A. Sadovskyy, L. B. Ioffe, A. Y. Kitaev, and M. E. Gershenson, *Quantum Superinductor with Tunable Nonlinearity*, Phys. Rev. Lett. **109**, 137003 (2012).

[38] J. Koch, T. M. Yu, J. Gambetta, A. A. Houck, D. I. Schuster, J. Majer, A. Blais, M. H. Devoret, S. M. Girvin, and R. J. Schoelkopf, *Charge-Insensitive Qubit Design Derived from the Cooper Pair Box*, Phys. Rev. A **76**, 042319 (2007).

[39] J. J. Burnett, A. Bengtsson, M. Scigliuzzo, D. Niepce, M. Kudra, P. Delsing, and J. Bylander, *Decoherence Benchmarking of Superconducting Qubits*, npj Quantum Inf. **5**, 54 (2019).

[40] A. Osman, J. Simon, A. Bengtsson, S. Kosen, P. Krantz, D. P. Lozano, M. Scigliuzzo, P. Delsing, J. Bylander, and A. Fadavi Roudsari, *Simplified Josephson-Junction Fabrication Process for Reproducibly High-Performance Superconducting Qubits*, Appl. Phys. Lett. **118**, 064002 (2021).

[41] C. K. Andersen and A. Blais, *Ultrastrong Coupling Dynamics with a Transmon Qubit*, New J. Phys. **19**, 023022 (2017).

[42] J. T. Shen and S. Fan, *Strongly Correlated Multiparticle Transport in One Dimension through a Quantum Impurity*, Phys. Rev. A **76**, 062709 (2007).

[43] J. Puertas Martínez, S. Léger, N. Gheeraert, R. Dassonneville, L. Planat, F. Foroughi, Y. Krupko, O. Buisson, C. Naud, W. Hasch-Guichard, S. Florens, I. Snyman, and N. Roch, *A Tunable Josephson Platform to Explore Many-Body Quantum Optics in Circuit-QED*, npj Quantum Inf. **5**, 19 (2019).

[44] N. M. Sundaresan, Y. Liu, D. Sadri, L. J. Szocs, D. L. Underwood, M. Malekakhlagh, H. E. Türeci, and A. A. Houck, *Beyond Strong Coupling in a Multimode Cavity*, Phys. Rev. X **5**, 021035 (2015).

[45] V. S. C. Manga Rao and S. Hughes, *Single Quantum-Dot Purcell Factor and β Factor in a Photonic Crystal Waveguide*, Phys. Rev. B **75**, 205437 (2007).

[46] P. Solinas, M. Möttönen, J. Salmilehto, and J. P. Pekola, *Decoherence of Adiabatically Steered Quantum Systems*, Phys. Rev. B **82**, 134517 (2010).

[47] A. J. Kollár, M. Fitzpatrick, and A. A. Houck, *Hyperbolic Lattices in Circuit Quantum Electrodynamics*, Nature (London) **571**, 45 (2019).

[48] P. Longo, P. Schmitteckert, and K. Busch, *Few-Photon Transport in Low-Dimensional Systems*, Phys. Rev. A **83**, 063828 (2011).

[49] M. Hafezi, D. E. Chang, V. Gritsev, E. Demler, and M. D. Lukin, *Quantum Transport of Strongly Interacting Photons in a One-Dimensional Nonlinear Waveguide*, Phys. Rev. A **85**, 013822 (2012).

[50] Z. Wang, T. Jaako, P. Kirton, and P. Rabl, *Supercorrelated Radiance in Nonlinear Photonic Waveguides*, Phys. Rev. Lett. **124**, 213601 (2020).

[51] I. Carusotto, D. Gerace, H. E. Tureci, S. De Liberato, C. Ciuti, and A. Imamoğlu, *Fermionized Photons in an Array of Driven Dissipative Nonlinear Cavities*, Phys. Rev. Lett. **103**, 033601 (2009).

[52] D. E. Chang, V. Gritsev, G. Morigi, V. Vuletić, M. D. Lukin, and E. A. Demler, *Crystallization of Strongly Interacting Photons in a Nonlinear Optical Fibre*, Nat. Phys. **4**, 884 (2008).

[53] I. V. Pechenezhskiy, R. A. Mencia, L. B. Nguyen, Y.-H. Lin, and V. E. Manucharyan, *The Superconducting Quasicharge Qubit*, Nature (London) **585**, 368 (2020).

[54] N. Samkharadze, A. Bruno, P. Scarlino, G. Zheng, D. P. DiVincenzo, L. DiCarlo, and L. M. K. Vandersypen, *High-Kinetic-Inductance Superconducting Nanowire Resonators for Circuit QED in a Magnetic Field*, Phys. Rev. Applied **5**, 044004 (2016).

[55] A. Shearrow, G. Koolstra, S. J. Whiteley, N. Earnest, P. S. Barry, F. J. Heremans, D. D. Awschalom, E. Shirokoff, and D. I. Schuster, *Atomic Layer Deposition of Titanium Nitride for Quantum Circuits*, Appl. Phys. Lett. **113**, 212601 (2018).

[56] D. Niepce, J. Burnett, and J. Bylander, *High Kinetic Inductance NbN Nanowire Superinductors*, Phys. Rev. Applied **11**, 044014 (2019).

[57] L. Grünhaupt, M. Spiecker, D. Gusenkova, N. Maleeva, S. T. Skacel, I. Takmakov, F. Valenti, P. Winkel, H. Rotzinger, W. Wernsdorfer, A. V. Ustinov, and I. M. Pop, *Granular Aluminium as a Superconducting Material for High-Impedance Quantum Circuits*, Nat. Mater. **18**, 816 (2019).

[58] T. Weißl, B. Küng, E. Dumur, A. K. Feofanov, I. Matei, C. Naud, O. Buisson, F. W. J. Hekking, and W. Guichard, *Kerr Coefficients of Plasma Resonances in Josephson Junction Chains*, Phys. Rev. B **92**, 104508 (2015).

[59] C. Eichler and A. Wallraff, *Controlling the Dynamic Range of a Josephson Parametric Amplifier*, Eur. Phys. J. Quantum Technol. **1**, 2 (2014).

[60] A. Lai, T. Itoh, and C. Caloz, *Composite Right/Left-Handed Transmission Line Metamaterials*, IEEE Microw. Mag. **5**, 34 (2004).

[61] M. H. Devoret *et al.*, *Quantum Fluctuations in Electrical Circuits*, Les Houches, Session LXIII **7**, 133 (1995), https://boulderschool.yale.edu/sites/default/files/files/devoret_quantum_fluct_les_houches.pdf.

[62] F. Ciccarello, *Resonant Atom-Field Interaction in Large-Size Coupled-Cavity Arrays*, Phys. Rev. A **83**, 043802 (2011).

[63] S. Longhi, *Bound States in the Continuum in a Single-Level Fano-Anderson Model*, Eur. Phys. J. B **57**, 45 (2007).

[64] E. Shahmoon and G. Kurizki, *Nonradiative Interaction and Entanglement between Distant Atoms*, Phys. Rev. A **87**, 033831 (2013).

[65] D. F. Walls and G. J. Milburn, *Quantum Optics*, 2nd ed. (Springer-Verlag, Berlin, 2008).